Simulation of Space Environment Effects on Particle Sensors

by

Saeed ur Rehman

A thesis submitted in partial fulfillment of the requirements for the degree of

Doctor of Philosophy

Department of Physics
University of Alberta

Abstract

This dissertation presents detailed analyses of the interaction between space plasma and satellites, and its effect on the payload sensor measurements using particle in cell (PIC) and test-particle modeling. In a satellite frame, the plasma flow velocity $\vec{v}$ and geomagnetic field $\vec{B}$ lead to a motional electric field $\vec{E} = -\vec{v} \times \vec{B}$, which affects the sheath surrounding the spacecraft and the particle distribution functions in the vicinity of the sensors. Combined with the sheath electric field resulting from spacecraft charging, this can then lead to aberrations in measurements made with these sensors, particularly with those sensitive to thermal particles. As case studies, a particular attention is given to the Swarm electric field instrument (EFI). On each of the three Swarm satellites, EFI consists of a pair of thermal ion imagers (TIIs) mounted on the ram face and two small Langmuir probes extending in the nadir direction. The TIIs are capable of measuring ion distributions in three-dimensional velocity space. The centroid of the O^+ ion flux on the array of detectors in these sensors, serves to determine the plasma flow velocity in the satellite rest frame, from which the motional electric field can be inferred from the relation above. At the time of this writing, no in situ validated measurements were available from the Swarm sensors, but simulation results obtained, assuming representative ionospheric parameters, indicate that aberrations associated with spacecraft charging and motional electric fields can be expected to vary in the range ± 200 m/s between the North and South magnetic poles. Characteristics of the Langmuir probes are also calculated, in which the effect of the local magnetic field and the possibility of crosstalk is considered. Magnetic fields are found to have a measurable effect, despite the fact that thermal electrons have a larger gyro-radius than the probe size. Under normal conditions, no significant crosstalk between the

probes is expected. In another study, the first fully kinetic quantitative estimate of magnetic field perturbations caused by the interaction of a spacecraft with space environment is made. In this case, magnetic field perturbations are below the sensitivity threshold of the on-board Swarm magnetometers. However, for missions subject to more intense solar radiation, they would likely approach or exceed instruments' sensitivity thresholds. Finally, PTetra simulations are applied to a laboratory experiment, relevant to plasma-satellite interaction. In this experiment, the interaction of a supersonic argon plasma with a conducting sphere in a vacuum chamber is studied, and Langmuir probe characteristics are measured. Characteristics are computed at two probe locations which are in good agreement with measurements.

Preface

Most of the research results presented in this thesis has already been reported in referred scientific journals. Chapter 3 of this dissertation is based on two published papers as 1) S. Rehman, J. Burchill, A. Eriksson, and R. Marchand, "Earth magnetic field effects on Swarm electric field instrument," Planetary and Space Science, vol. 73, $145 - 150$ and 2) S. Rehman, R. Marchand, J. Berthelier, T. Onishi, and J. Burchill, "Earth magnetic field effects on particle sensors on LEO satellites," IEEE Transactions on Plasma Science, vol. 41, $3402 - 3409$. In the first paper, I carried out the simulations, analyzed the results, and wrote the manuscript under the supervision of Professor Richard Marchand. In this work I had discussions with Professors J. Burchill and A. Eriksson who suggested problems to be considered in the simulations. The geometry of the particle sensor was provided by J. Burchill. The second paper consists of two distinct parts; a part of it comprised of my work in which I was responsible for simulations, result analysis, and writing my half of the manuscript. Professor Richard Marchand discussed the interpretation of the simulation results with me, and wrote the second part of the paper. Note that only the part for which I was responsible is included in this thesis. The other co-authors contributed to the second part. Chapter 4 is based on a recently published letter as Saeed-ur-Rehman and Richard Marchand, "Plasma-satellite interaction driven magnetic field perturbations," Physics of Plasmas, vol. 21, 090701. The idea of this work was suggested by Professor Richard Marchand. I modified PTetra to do the first fully kinetic estimate of current density and

magnetic field perturbations associated with satellite-plasma interaction. I was also responsible for carrying out the simulations, writing the manuscript, and analyzing the result. The work presented in chapter 5 was done in collaboration with Lisa Gayetsky, a PhD student in Dartmouth college, USA. Ms. Gayetsky provided me with the geometry of the experimental set up, the value of the Earth magnetic field in the system of coordinates of the experiment, and several measured I-V characteristics. I constructed the simulation geometry, fitted probe characteristics, and computed plasma parameters. This work will soon be submitted for review.

To my Family

Acknowledgments

I am grateful to my supervisor Professor Richard Marchand for his continuous support and supervision during my PhD program. I would not have completed this thesis without his support and guidance. I am indebted to my supervisory committee members, Professor Massimo Boninsegni and Professor Richard D. Sydora, for their useful comments and interest throughout my PhD studies.

I would like to acknowledge my collaborators, Lisa Gayetsky, Johnathan Burchill, and Anders Eriksson, for the valuable discussion that we had in the Interaction of Satellites with Space Environment meeting at International Space Science Institute (ISSI), Bern Switzerland. Thanks to Lisa Gayetsky for exchanging emails and for sharing her experimental data throughout the collaboration.

A grateful smile to all of my friends and fellow graduate students, Salman, Nadia, Fahad, Sajjad, Asad, Asif, Khalil, Aziz, and Scott. The deepest gratitude goes to my sisters and brothers who helped me in one way or another. An immense thanks to my wife for being so encouraging and supportive. She always took my domestic responsibilities to let me concentrate on my studies and thesis write-up. It is a pleasure to express my profound love and thanks to my parents for their affection and best wishes for me. How can I forget my first day with them in the kindergarten and their inexhaustible support to educate me. All of this is possible due to their encouragement and support. I would

also like to thank all of my first teachers who contributed in educating me.

Thanks to the Department of Physics and my supervisor for their financial support through teaching and research assistantships. I am also indebted to the Pakistan Institute of Nuclear Science and Technology (PINSTECH), Pakistan for providing partial financial support.

Contents

List of Tables

List of Figures

List of Abbreviations

CHAWS	Charge Hazards and Wake Studies
DynaPAC	Dynamic Plasma Analysis Code
EFI	Electric field instrument
ESA	European Space Agency
EUV	Extreme ultraviolet
GEO	Geosynchronous Earth orbit
IGRF	International geomagnetic reference field
IRI	International Reference Ionosphere
I-V	Current-voltage
JAXA	Japan Aerospace Exploration Agency
LEO	Low Earth orbit
MCP	Micro channel plate
MSIS	Mass Spectrometer and Incoherent Scatter
MUSCAT	Multi-Utility Spacecraft Charging Analysis Tool
NASCAP	NASA Charging Analyzer Program
NASCAP/GEO	NASA Charging Analyzer Program for Geosynchronous Orbit
NASCAP/LEO	NASA Charging Analyzer Program for Low-Earth Orbit
OML	Orbital motion limited
PE	Photoemission
PEO	Polar Earth orbit
PIC	Particle in cell
POLAR	Potentials of Large Objects in the Auroral Region
SPIS	Spacecraft Plasma Interaction Software
SPP	Solar Probe Plus
TII	Thermal ion imager
UV	Ultraviolet
WSF	Wake Shield Facility

Chapter 1

Introduction

1.1 Plasma-satellite interaction

The interaction of a planetary magnetosphere or solar wind plasma with a space vehicle is referred to as plasma-satellite interaction. In the interaction, a number of physical processes are occurring. For example, charged particles incident on a satellite surface can be absorbed or reflected, photo-electrons can be emitted due to incident solar ultraviolet (UV) photons, secondary electrons can be emitted at the surface, following incident high energy electrons or protons, and current is flowing between the conducting surfaces etc. Figure 1.1 illustrates the main processes involved in spacecraft charging. At steady state, a satellite collects zero net current (I_{net}), which is represented by the fundamental equation of spacecraft charging

$$I_{net} = \sum I_{in} + \sum I_{out} = 0, \tag{1.1}$$

where $\sum I_{in}$ and $\sum I_{out}$ are the summation of all incoming and outgoing currents respectively. All of the above mentioned processes lead to satellite charging with a net charge that is either positive or negative, depending on their relative importance. The details of spacecraft charging mechanism are given in

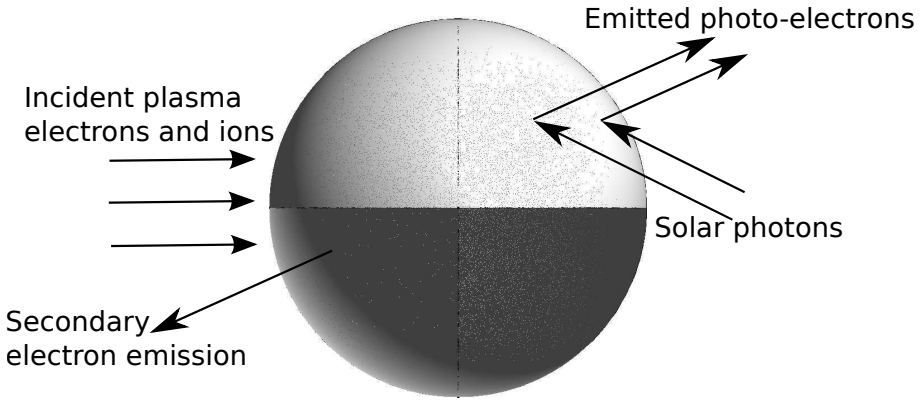

Figure 1.1: Illustration of the various charging processes of a spherical satellite in space plasma.

a number of articles and books [1, 2, 3, 4, 5, 6]. A charged satellite will then perturb the surrounding environment, which will then form an electric sheath surrounding the satellite, and thus perturb charged particle sensor measurements. In the following paragraphs, a review of selected studies of spacecraft charging and resulting sheath effects is presented.

1.2 Review of earlier work

Langmuir was the first to show that a body immersed in a plasma becomes electrically charged as a result of its interaction with it [7, 8]. He introduced a method to determine the plasma density and temperature, two basic plasma parameters, from measured current-voltage (I-V) characteristics of a conducting probe. He mostly worked on planar, cylindrical, and spherical probes which are still widely used to measure in situ plasma parameters both in space and laboratory applications. The first paper describing charging of a dust particle in interstellar space was published by Jung in 1937 [9]. The author assumed photo-emission as a dominant process and concluded that dust particles must be positively charged. Spitzer in 1941, considered the same problem with more realistic yields of photo-electron emission, and concluded that dust grains had to be charged to a negative potential of -2 V, independently of their radius

[10]. This is due to the higher collection rate of incident fast moving electrons than photo-electric ionization. His later work showed that a metallic grain may have positive potential, if photo-emission is significant [11]. In 1956, Lehnert calculated the floating potential of a spherical satellite to be about -0.7 to -1 V corresponding to the electron temperature 1 eV at altitude of 500 km [12]. He found that a negatively charged satellite repels electrons along the magnetic field lines, which are nearly perpendicular to its drift velocity. Gringauz and Zelikman in 1957 derived an equation for the equilibrium satellite potential in anticipation of the Sputnik [13]. In their calculations, they took into account the satellite's drift velocity and photo-emission and estimated the potential gradient generated by the satellite's motion in Earth's magnetic field. Imyanitove estimated the sheath electric field associated with the charged satellite [14]. He mentioned that to determine the ionospheric electric field the sheath field must be accounted for in the measured field. An article entitled "Charge and Magnetic Field Interaction with Satellites" was published by Beard and Johnson in 1960 [15]. A satellite motion across the geomagnetic field induces an electric field in its frame, called motional electric field. This field could be as high as 0.2 V/m, and may cause abberation in the measured satellite potential [15]. A magnetic field decreases a body's effective collection area in a plasma by restricting particle motion, especially electrons, to be along the field line [16]. Rocket charging was reported in the 1960's [17, 18, 19]. Applications Technology Satellite (ATS) 5 charging in synchronous orbit was reported by DeForest [20]. The observations showed ATS charging to higher negative voltages during eclipse, due to the absence of photo-electron emission.

In parallel with analytical calculations, in situ observations, and laboratory measurements, a need was soon identified to develop computer codes for understanding of plasma-satellite interaction and the various charging processes responsible for the observed anomalies on geosynchronous spacecraft. In the

seventies, a joint effort between NASA and the U.S. Air Force was initiated to develop several computer models. These are NASA Charging Analyzer Program for Geosynchronous Orbit (NASCAP/GEO), NASA Charging Analyzer Program for Low Earth Orbit (NASCAP/LEO), Potentials of Large Objects in the Auroral Region (POLAR), and Dynamic Plasma Analysis Code (DynaPAC). These models were later integrated into a single model called NASCAP (NASA Charging Analyzer Program) [21], and since then it has been the main simulation tool used in the U.S. to model the interaction between spacecraft and the space environment. The first studies made with NASCAP mainly focused on the charging of geosynchronous satellites [22, 23], which can reach high voltages. The flight experiment Charge Hazards and Wake Studies (CHAWS) was flown on the Wake Shield Facility (WSF) [24]. In this experiment, the current collection by a negatively biased cylindrical probe in the wake of WSF was studied to enhance the knowledge of the wake structure behind a spacecraft and measure the ion current in the wake. The Dynamic Plasma Analysis Code (DynaPAC), an older version of the Nascap-2k, was used to simulate the CHAWS experiment, and its results provided direct comparisons with measurements [25]. For probe biasing voltages $V_{bias} < -100$ V, the measured collected current agreed with the simulated current. For less negative bias voltages $-100V < V_{bias}$, however, the computed current was much less than the actual measured current. Their interpretation for this discrepancy between observation and model prediction was attributed to the presence of smaller mass ionospheric hydrogen ions, spacecraft thrusters, and increased plasma density in the wake due to outgassing; these factors not being taken into account in the model. More details about this study can be found in the above cited articles. NASCAP has been continuously upgraded, and its latest version is known as Nascap-2k [26]. It can simulate environment-satellite interaction from low Earth orbit (LEO) to interplanetary missions. For example, spacecraft interaction with tenuous plasma in geosynchronous Earth orbit (GEO) and solar

wind environments was modeled with Nascap-2k [27]. In this study, the model capabilities were demonstrated by simulating the Defense Satellite Communication System (DSCS-III), STEREO spacecraft, and MESSENGER, a mission to Mercury. STEREO spacecraft potential variations with solar wind density, electron temperature, and cover-glass conductivity were modeled successfully. Also, the MESSENGER potential field is found to perturb the on-board ion detector measurement. In another study by Donegan [28], the effects of extreme environments in space (near the sun) on pyrolytic born nitride, barium zirconium phosphate and Al_2O_3 materials were studied using Nascap-2k. It was found that absolute and differential surface charging are functions of temperature and radiation fluxes. This study revealed that among the materials considered, Al_2O_3 coatings minimize both absolute and differential spacecraft charging.

Other models used for studying the interaction of spacecraft with space environment are Spacecraft Plasma Interaction Software (SPIS) [29] and Multi-Utility Spacecraft Charging Analysis Tool (MUSCAT) [30]. SPIS and MUSCAT were developed under contract from the European Space Agency (ESA) and the Japan Aerospace Exploration Agency (JAXA) respectively. SPIS simulations were used to investigate wake effects on the sheath region around the DEMETER satellite [31]. It was found that fast moving electrons make the wake region more negative and that the sheath can extend up to 2.5 meters in the wake region. The authors noted that the sheath around the spacecraft looked like a peach. The interaction of solar wind with Solar Probe Plus (SPP) spacecraft was simulated by SPIS model [32, 33]. The SPP is a NASA mission to study the near sun environment and gain a better understanding of the solar wind origination and acceleration. It will be the first space vehicle in history of mankind to reach so close to the sun (at a distance of 8.5 solar radii from the photosphere). SPIS simulations showed that SPP will be charged negatively,

to a potential ranging from −10 to −20 V, despite large photo-electron emitted currents and high secondary electron yields. The explanation for this is that the electrostatic barrier surrounding the surfaces emitting the electrons reflects emitted particles back to the surfaces. The formation of the barrier is explained in the articles [32, 33]. This negative biasing will affect measurements made with on-board particle sensors, and it will filter out the low energy electrons. In another article [34], a cross-comparison of MUSCAT code with SPIS and Nascap-2k was made by modeling a wake structure behind a drifting spacecraft in a dense and low temperature plasma. The spacecraft was in the form of a plate and its wake side was biased to −500 V whereas the ram side was kept at 0 V. The predicted current collected by the spacecraft was obtained from each of the code, and it was consistent with measurements made in a laboratory experiment. Also, their simulated plasma potentials are in good agreement. This study showed the power of these models of predicting the similar results although they are using very different numerical algorithms. In a recent article by Marchand, et al. [35], a cross comparison of various spacecraft charging models is explored. These models were 1) EMSES, 2) iPic3D, 3) LASP, 4) SPIS, and 5) PTetra. They simulated SPP interaction with solar wind near perihelion by taking into account the representative space environment conditions. A comparison of the spacecraft floating potential, ion and electron density, and the contribution of various emitted and collected current by the spacecraft was studied for four different scenarios. The models predicted the potential barrier formation around SPP and its floating potential to be −10 V. This study demonstrated the models capabilities and skill for modeling a spacecraft-plasma interaction in an extreme condition.

1.3 Space environment for satellites

The space environment for a satellite orbiting around Earth depends on the type of its orbit, altitude, and on whether it is in eclipse or exposed to solar radiation. For example, LEO (corresponds to altitudes between 200 km and 2000 km) satellites encounter a cold and dense plasma environment with a significant density of neutral particles while satellites in GEO (corresponds to an altitude of $\sim$ 36000 km) mostly interact with hot and tenuous plasma environment in which neutral particles are negligible. Satellites in PEO pass through auroral regions (latitudes $> 65^{\circ}$) and encounter energetic electrons and various ion species in contrast to low to mid-latitude LEO satellites. At low latitudes most of the incoming solar particles are blocked by the magnetosphere, and only solar radiation reaches the ionosphere. High energy particles and radiation (UV, EUV, and X-rays) often cause electron emission from a satellite surfaces, which further contribute to the physics of interaction between spacecraft and the space environment.

Representative space plasma parameters relevant to LEO can be obtained from the International Reference Ionosphere (IRI) model. For example, Fig. 1.2 shows the electron density profile above the (magnetic) North pole. The density increase in the F layer at an altitude of approximately 330 km is clearly visible in the figure. Ionospheric ion density variations with altitude are shown in Fig. 1.3. LEO and PEO satellites are affected by atmospheric drag because of the relatively high neutral density at these altitudes. Neutral densities are very low at GEO altitudes and their effect on satellites is negligible. Their concentrations relative to altitude are calculated with the Mass Spectrometer and Incoherent Scatter (MSIS) model and shown in Fig. 1.4. The neutral temperature in the ionosphere for the above mentioned conditions varies from 0.01 eV to 0.1 eV according to the MSIS model.

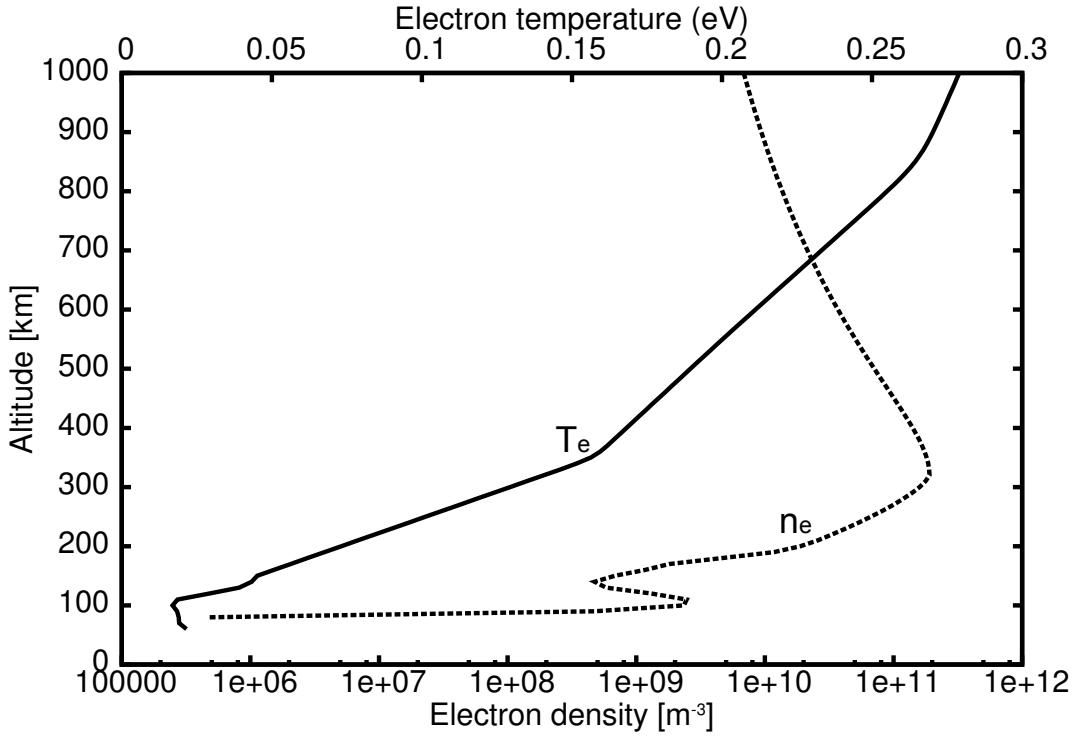

Figure 1.2: Electron density (n_e) and temperature (T_e) profiles in the ionosphere. These plots were generated with the IRI model assuming a latitude of 86°, longitude of 213°, January 01, 2014, local noon, and quiet solar conditions. The latitude and longitude correspond to the approximate position of the North magnetic dip pole at present, where the geomagnetic field vector exactly points in the nadir direction, i.e., directed perpendicularly to Earth's surface.

1.4 Swarm mission

A major contribution of this thesis is the study of the physics of spacecraft interaction with space environment, with a special emphasis on its effect on particle sensors. For that purpose, sheath effects on the Swarm electric field instrument (EFI) is simulated and studied in detail.

Swarm is the latest in a series of space missions aimed at monitoring the Earth's magnetic field [36, 37]. Precise mapping of the geomagnetic field and measuring its temporal variations is needed in the understanding of the geodynamo. It is also needed in the study of the interplay between the Sun and Earth

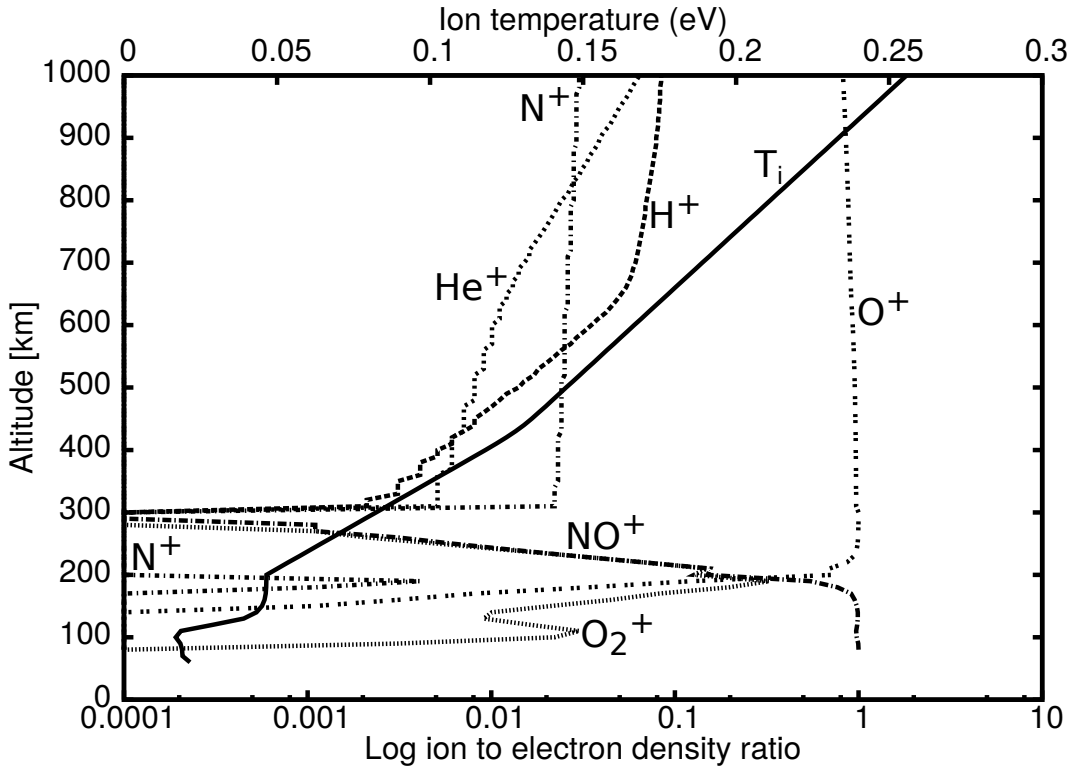

Figure 1.3: Ion density and temperature profiles in the ionosphere. These plots were generated with the IRI model assuming a latitude of 86°, longitude of 213°, January 01, 2014, local noon, and quiet solar conditions. The latitude and longitude correspond to the approximate position of the North magnetic dip pole at present.

near-space environment. Swarm was preceeded by the Magsat [38], Ørsted [39], and CHAMP [40]. These missions provided essential data in the development and updating of geomagnetic field models such as CHAOS [41] and the IGRF [42]. In addition to fundamental geophysics and space physics, these measurements are of interest from a broader planetary and societal perspective. Indeed recent observations reveal that the strength of Earth's magnetic field is decreasing in the bottom of the South Atlantic Ocean [43, 42], and the North magnetic dip pole is moving at a speed of $\sim$ 50km/yr from the Canadian arctic toward Siberia [44, 45, 42]. Palaeomagnetic studies at the Steens mountains revealed that the geomagnetic field changes rapidly during a polarity transition [46]. Concurrently, geomagnetic poles wandering, and reversal of the dipole polarity

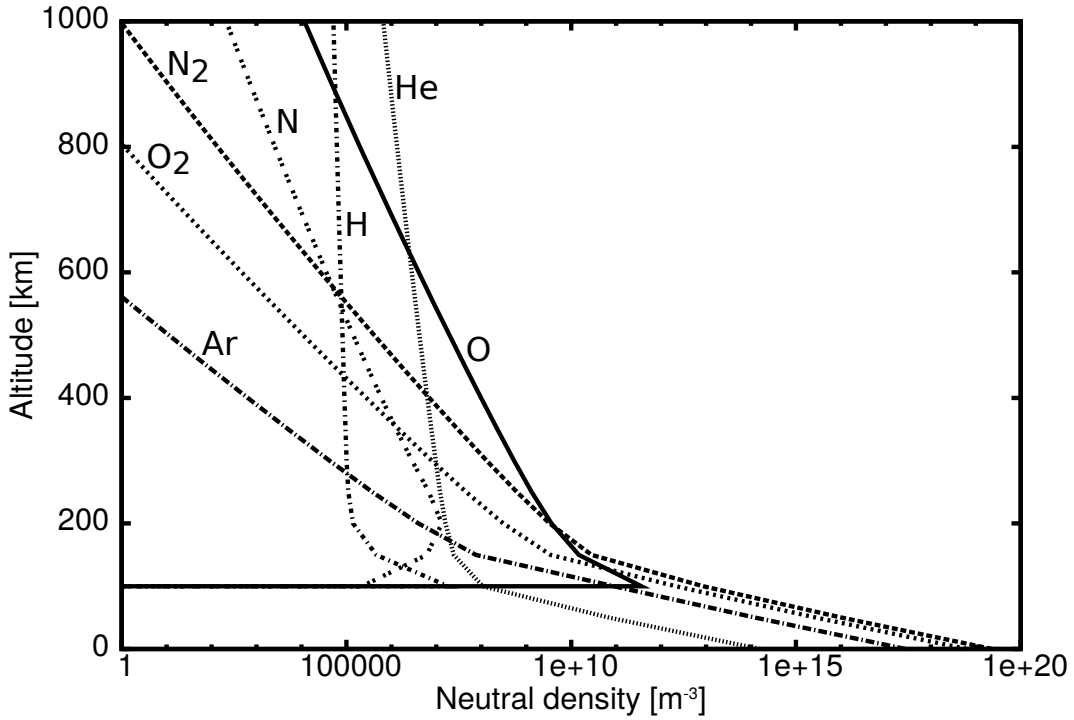

Figure 1.4: Neutral particle concentrations as a function of altitude at the North dip pole location. These plots are generated with the MSIS model for winter and quiet solar conditions.

were also simulated numerically [47]. Based on this understanding, it has been suggested that the observed changes might correspond to the initial phase of a pole reversal [48, 49, 43]. A weakening of the field, whether transient or associated with pole reversal, would expose the upper atmosphere to higher levels of radiation. In addition to increased health hazard to crew and passengers in flights in the upper parts of the troposphere, global changes in the geomagnetic field would affect the penetration of ionizing particles in the atmosphere. This in turn would impact the formation of clouds and it might lead to long-term climate changes [50, 51].

The Swarm mission, a constellation of three identical satellites (Fig. 1.5) was launched from Plesetsk Cosmodrome, Russia on November 22, 2013 [52], with the objective of quantifying Earth's magnetic field contributions from the

geodynamo, the ionosphere and magnetosphere, oceanic and atmospheric currents and their variations in time [36]. Each satellite carries many instruments

Figure 1.5: An artist's view of the three Swarm satellites in orbits. Two of the satellites are flying side by side at initial altitude of 460 km, whereas the third is orbiting at an altitude of 530 km. All three satellites have quai-polar circular orbits. The image is reprinted with permission from the ESA website.

and electrical components on a payload exceeding nine meters in length as shown in Fig. 1.6, the details of the instruments studied in this thesis will be presented later in the relevant chapters.

1.5 Motivation and objectives of the present work

Satellites have been in use for telecommunications, meteorology, geodesy, Earth observation for both civilian and military purposes, studying the Solar system,

its planet, and the search for life outside of planet Earth etc. They are now an indispensable part of our well being and safety. A satellite surface and on-board sensors are always in contact with its outer environment, e.g., charged particles, neutral particles (important only for LEO satellite), and radiation. This interaction perturbs the surrounding space environment and may cause adverse effects. For example, 1) it may cause the malfunction of a space vehicle in extreme charging and discharging events and 2) it affects the measurements of the sensors mounted on the payload. As our knowledge of the outer space relies on accurate measurements and the correct interpretation of these sensor data, understanding plasma-satellite interaction and determining its effect on the on-board scientific instruments is critical. For these reasons, I devoted a large fraction of my thesis work to study the interaction between space plasma and the Swarm satellites, with a particular attention to TIIs and Langmuir probes that are part of the EFI instrument. I also considered possible magnetic field perturbations in the vicinity of the vector and scalar Swarm magnetometers to assess the magnitude of possible perturbation that could interfere with measured fields of geophysical origin. My specific objectives in this work are:

- to make a quantitative assessment of aberrations in measured ionospheric plasma flow velocities associated with sheath effects in the presence of a geomagnetic field.
- Study Swarm-plasma interaction effect on the Langmuir probes characteristics and finding the mutual coupling between the probes.
- Make quantitative estimates of magnetic field perturbations induced by the plasma-satellite interaction.

Furthermore, a laboratory experiment, aimed to gain a better understanding of the spacecraft-plasma interaction, is also modeled. The goals are:

- to compute the Langmuir probe characteristics and compare with measurements.

- to determine the experimentally unknown plasma parameters via simulations and assess the validity of the technique used by the experimentalists to infer these parameters.

These studies address questions that are timely and of significant interest to the space community. Also, these studies are intended to improve our understanding of the interaction between spacecraft and the space environment.

1.6 Thesis outline

The reminder of my thesis is organized as follows.
Chapter 2 describes the basic principles of the numerical models, specifically, the general approach used in PTetra and in test-kinetic simulations are reviewed. Geomagnetic field effects on EFI measurements are investigated in Chapter 3. This chapter is based on two peer reviewed journal articles [53, 54]. In chapter 4, a quantitative estimate of the magnetic field perturbations associated with plasma-satellite interaction is made for the Swarm satellites. This work is based on a recently published letter [55]. Modeling results of a laboratory experiment are presented in chapter 5. In the study, the simulated I-V characteristics are compared with experimental results. This work is intended to be submitted for publication in a specialized refereed journal. Chapter 6 is devoted to a summary and conclusion of the thesis.

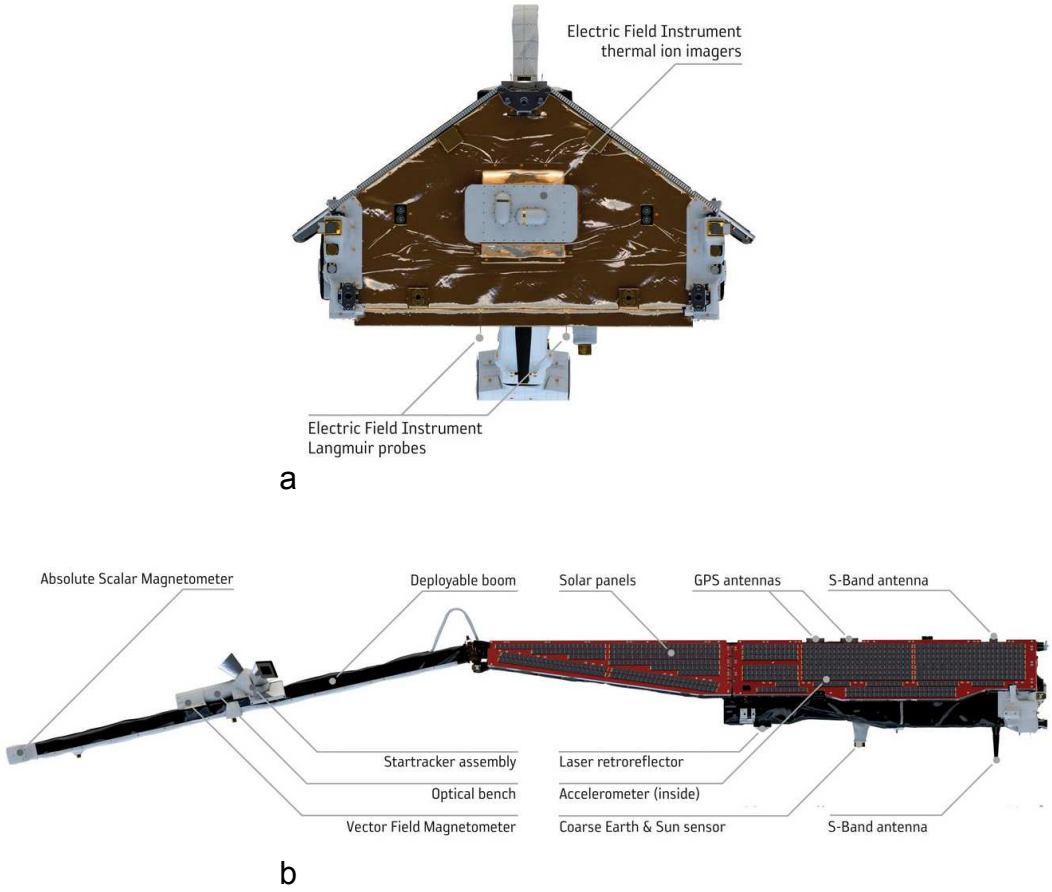

Figure 1.6: General overview of Swarm satellite instruments and their locations. The electric field instrument (EFI) made of two thermal ion imagers (TIIs) and two spherical Langmuir probes is shown in panel a. Panel b displays various electrical components, sensors, and detectors carried by each Swarm satellite. In this dissertation, plasma-satellite interaction effects on the EFI and both magnetometers (vector and scalar) are studied. These images are reprinted with permission from the ESA website.

Chapter 2

Computational framework

In this thesis, a plasma kinetic model is used to study the interaction of space plasma with a satellite and its instruments, and its effect on their measurements. Kinetic simulations are needed because the space plasma considered are nearly collisionless. As a result, a fluid or multiple moment approach would not be applicable. The general strategy used throughout this work is described in detail in the following.

2.1 Geometry and space discretization

The starting point for studying plasma interaction with a satellite, its probes and sensors is the construction of a geometry. The interacting body is enclosed in a simulation box as displayed in Fig. 2.1; its shape varies from case to case depending on the nature of the study. The space between the simulation box and the satellite is discretized with an unstructured tetrahedral mesh whereas a triangular mesh is used to represent the satellite surface and the outer boundary of the simulation domain. The gmsh mesh generator is used in this study. Gmsh is a finite element mesh generator developed by Christophe Geuzaine and Jean-Francois Remacle [56]. This software includes several modules that can be used to construct a geometry, as well as two and three dimensional meshes. It can

also be used to carry out a full simulation. In this study, only the geometry and mesh generation modules are used. All geometrical and mesh instructions are prescribed either interactively using the graphical user interface or in text files using the gmsh scripting language.

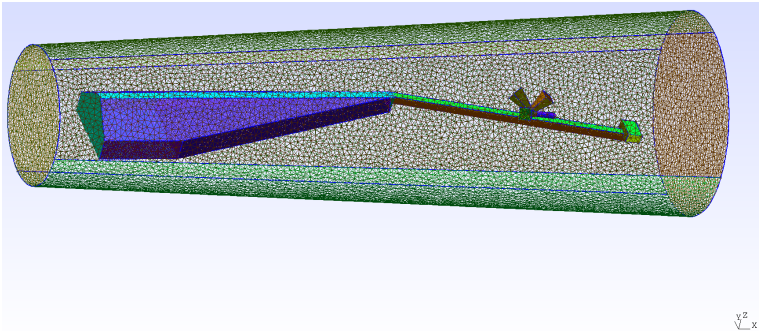

Figure 2.1: Illustration of the simplified Swarm geometry constructed in gmsh. The simulation domain is delimited by an outer boundary consisting of a truncated cone. Here, only the surface mesh is shown for clarity.

2.2 Kinetic modeling with PTetra

PTetra is one of several spacecraft-plasma interaction models; it was developed by R. Marchand [57]. It uses an adaptive unstructured tetrahedral grid capable of representing boundaries with complex or irregular shapes. It also uses this grid to solve for the electrostatic potential and associated electric fields from a finite element discretization of Poisson's equation. At present, the code is electrostatic; but it accounts for a time-independent and uniform magnetic field. In addition, it can compute first order magnetic field perturbations. It may account for an arbitrary number of species with different densities, masses, charges, temperatures, and drift velocities. Each ion species is characterized by a charge and a mass. It describes all particle species fully kinetically with physical masses and charges. It includes processes like photo-emission and secondary emission. The approach used in PTetra and some of its features are described below.

2.3 The PIC approach in PTetra

PTetra uses a standard particle in cell (PIC) approach as described in [58, 59]. In this approach, macro particles which are much fewer in number than actual particles in the system are simulated. Each macro particle carries a statistical weight which is chosen such that it represents the actual number of physical particles. The numerical particles contribute to a charge assigned to each vertex of the element (tetrahedron) in which they are located. The fraction of the particle assigned to each vertex is computed from a linear interpolation between vertices and the position of the particle.

2.3.1 Particle density

In PIC modeling, particle numbers and charge densities are calculated at grid points from their discrete positions. Each particle in the system is assigned in part to the vertices of the tetrahedron in which it is located. The fraction of a particle assigned to a vertex is given by the value of the linear interpolating function (ψ_j) which is equal to unity at that vertex and zero at other vertices as

$$\psi_j = \begin{cases} 1 & \text{at vertex j of cell } k, \\ 0 & \text{at other vertices of cell } k. \end{cases}$$

It is important to mention that in a given tetrahedron, the sum of the fractions assigned to the four vertices is equal to one, so that particles are neither destroyed nor created. This function is defined in terms of four parameters a, b, c, and d as

$$\psi_j = ax + by + cz + d, \tag{2.1}$$

these parameters are determined algebraically for each cell from the four conditions at the vertices of a tetrahedron mentioned above. In PTetra, the contribution to the particle density at node j, from particles located in a tetrahedron

k is given by

$$n_j = \sum_i \frac{w_i[1 + (\vec{r_i} - \vec{r_j}) \cdot \nabla\psi_j]}{V}, \tag{2.2}$$

where w_i and V are the statistical weight of the macro particle and the volume of Voronoi cell associated with vertex j respectively. The summation is over the total number of particles in cell k. Here, $\vec{r_i}$ is the position vector of particle i in the cell whereas $\vec{r_j}$ is the position vector of vertex j of the cell. Referring to Eq. 2.1, the gradient of ψ_j is given as

$$\nabla\psi_j = (a, b, c). \tag{2.3}$$

In order to obtain the charge density, the summand in right hand side of Eq. 2.2 is multiplied by the charge of a particle q_i. Thus, the linear interpolating functions connect the particle quantities with grid points.

2.3.2 Simulation timestep

A simulation timestep of PTetra is based on a combination of the fastest particle speed, the minimum Voronoi cell volume, the plasma, and gyro frequencies. In the code, one may specify an arbitrary number of ion and electron species. An estimate of the maximum speed for each species (electrons or ions) is made from the expression

$$v_{ik} = v_{tik} + v_{dik}. \tag{2.4}$$

The subscripts t and d in Eq. 2.4 indicate thermal and drift respectively. In the presence of photo-emission, the largest electron speed is the maximum of the speeds calculated from Eq. 2.4, and that of a representative photo-electron (corresponding to $1 - 3$ eV). Given the largest speed v_f between all electrons and ions, the simulation timestep is calculated as

$$\Delta t_v = \epsilon_{\Delta t} \frac{(V_{min})^{1/3}}{v_f}. \tag{2.5}$$

Here V_{min} is the smallest volume of the Voronoi cells in the mesh whereas $\epsilon_{\Delta t}$ is a timestep scaling factor, which is a parameter in the input file, used to fine-tune the simulation timestep. For example, considering that the smallest Voronoi cell can be significantly smaller than the average Voronoi cell, and that these cells are typically very few in number, it is usually acceptable to use a scaling factor $\epsilon_{\Delta t} > 1$. The time scales associated with the electron plasma frequency and the cyclotron frequency are calculated as

$$\Delta t_{\omega_p} = \varepsilon_{\omega_p} \frac{2\pi}{\omega_p}, \tag{2.6}$$

$$\Delta t_{\Omega} = \varepsilon_{\Omega} \frac{2\pi}{\Omega}, \tag{2.7}$$

and compared with Δt_v to choose the smallest timestep for simulation. The plasma frequency ω_p and the electron gyro frequency Ω_e are defined by

$$\omega_p = \sqrt{\frac{n_e e^2}{m_e \epsilon_0}}, \tag{2.8}$$

$$\Omega = \frac{eB}{m_e}. \tag{2.9}$$

The symbols n_e, m_e, e, ϵ_0, and B are the total electron density summed over all electron species, the electron mass, unit charge, the permittivity of vacuum, and a magnetic field respectively. Fraction factors (ε_{ω_p} and ε_{Ω}) are selected in order to ensure the stability condition ($\omega \Delta t \leq 0.3$) [58, 59].

2.3.3 Particle trajectories

The following equations are solved for calculating particles' position, velocity, and electric field at each timestep.

$$m \frac{d\vec{v}}{dt} = q(\vec{E} + \vec{v} \times \vec{B}), \tag{2.10}$$

$$\frac{d\vec{r}}{dt} = \vec{v}, \tag{2.11}$$

$$\nabla^2\phi = -\frac{\rho}{\epsilon_0}. \tag{2.12}$$

In the above expressions, $m, q, \vec{r}$, and $\vec{v}$ are the mass, charge, position vector, and velocity of a particle respectively while $\vec{E}$ and $\vec{B}$ are electric and magnetic field vectors. In Eq. 2.12, ρ is the volume charge density and ϕ is the scalar potential. The equations of motion (2.10 and 2.11) are discretized using a second order leapfrog scheme [58, 59]. In this method, particle positions are calculated at integral timesteps while velocities are computed at half-integral timesteps. For ions, Eqs. 2.10 and 2.11 are discretized as

$$\vec{v}_{t+\frac{\Delta t}{2}} = \vec{v}_{t-\frac{\Delta t}{2}} + \frac{q\Delta t}{m}(\vec{E}_t + \vec{v}_{t-\frac{\Delta t}{2}} \times \vec{B}_t), \tag{2.13}$$

$$\vec{r}_{t+\Delta t} = \vec{r}_t + \vec{v}_{t+\frac{\Delta t}{2}}\Delta t. \tag{2.14}$$

For electrons, the semi-implicit (using both previous and updated velocity in the right hand side) integration scheme is implemented rather than the explicit (using only previous velocity) one as done in Eq. 2.13. The discretization of Eq. 2.10 then becomes

$$\vec{v}_{t+\frac{\Delta t}{2}} = \vec{v}_{t-\frac{\Delta t}{2}} + \frac{q\Delta t}{m}(\vec{E}_t + \frac{\vec{v}_{t-\frac{\Delta t}{2}} + \vec{v}_{t+\frac{\Delta t}{2}}}{2} \times \vec{B}_t). \tag{2.15}$$

Equation 2.15 can be formulated as a matrix equation

$$\vec{v}_{t+\frac{\Delta t}{2}} = [I - \frac{\alpha R}{2}]^{-1}[I + \frac{\alpha R}{2}]\vec{v}_{t-\frac{\Delta t}{2}} + [I - \frac{\alpha R}{2}]^{-1}\alpha\vec{E}, \tag{2.16}$$

where $\alpha = -\frac{q\Delta t}{m_e}$; the I and R are the identity and so-called "rotation" matrices respectively.

$$I = \begin{bmatrix} 1 & 0 & 0 \\ 0 & 1 & 0 \\ 0 & 0 & 1 \end{bmatrix}, R = \begin{bmatrix} 0 & B_z & -B_y \\ -B_z & 0 & B_x \\ B_y & -B_x & 0 \end{bmatrix}.$$

Note that due to ions smaller gyro frequency, the semi-implicit formulation is not needed when solving ion equations of motion. In problems with a strong magnetic field, the maximum timestep chosen by the code is such that one electron gyration takes 10 timesteps or more per gyro cycle. Due to the large ion to electron mass ratio, however, Δt will always be such that it will take many more steps (more than $1,800$) to complete an ion gyro period. For heavier ions like Oxygen, gyration period is almost $30,000$ time larger than that of an electron.

2.3.4 Boundary conditions and fields

Dirichlet boundary conditions are used to solve Poisson's equation in PTetra. In the absence of a background magnetic field, the potential at the outer boundary is set to zero. In the presence of a magnetic field, there may be a potential gradient in the satellite frame of reference associated with the convection electric field $\vec{E} = -\vec{v} \times \vec{B}$, where $\vec{v}$ and $\vec{B}$ are plasma flow velocity and background magnetic field respectively. The potential at the boundary is then specified as $\phi_0 = \vec{v} \times \vec{B} \cdot \vec{r}$. The satellite is subdivided into surface components representing different physical objects on which different boundary conditions can be applied. For example, they may be 1) floating, 2) biased with respect to a reference, and 3) such as to collect a fixed amount of current. On each surface component "α" of the satellite, the potential ϕ_α is determined from all collected charges, the volume charge density (ρ), the potential at the outer boundary, and the capacitance matrix. Details of this calculation are given in an article by Marchand [57]. Poisson's equation (Eq. 2.12) is solved using the method of finite elements with a Taylor Galerkin discretization [60]. The resulting system of linear equations is characterized by a large sparse matrix

equation. The solution is obtained numerically using GMRES iterations with Saad's incomplete LU preconditioning [61]. The calculation of the electric fields are fully self-consistent, in that the fields are fed back in the calculation of particle trajectories. While the code is electrostatic, it can be used to estimate first order magnetic field perturbations. One of my contributions in this work was to modify PTetra to calculate the plasma current density and associated magnetic field perturbations. The current density ($\vec{J}$) is calculated from the computed velocity distributions of the particles. Using the Biot-Savart law, first order field perturbations can then be estimated from

$$\vec{B}(\vec{r}) = \frac{\mu_0}{4\pi} \int \vec{J}(\vec{r}) \times \frac{\vec{r} - \vec{r}}{\mid \vec{r} - \vec{r} \mid^3} d^3\acute{r}. \tag{2.17}$$

Field perturbations can also be computed from currents collected and circulating in the satellite itself.

2.3.5 Input and output

At the time of writing this dissertation, there are three input data files to PTetra. These are pictetra.dat, sc_materials.dat, and meshpic.dat. pictetra.dat is used to specify all the physical parameters of a simulation, such as the number of species, the density, and temperature of each species. It is also used to specify certain parameters to control the numerical flow of a simulation such as number of macro particles, the simulation time, and Poisson's equation solution method (GaussSeidel or YousefSaad_GMRES). The file contains detailed documentation for each parameter. The sc_materials.dat file is used whenever there is photo-electron or secondary electron emission from the satellite surfaces. It contains the details of material types, their work functions, most probable photo-electron energies, and saturation current densities. These data are used to compute the rate of electron emissions as a function of solar illumination and energetic electron flux. The file meshpic.dat contains the mesh details such

as coordinates of the grid points, vertices of the tetrahedrons, and their connectivity. It is needed to compute physical quantities at the grid points and in the tetrahedrons. The code periodically produces output files; details of these are summarized in table 2.1. The results of .vu and .vtk files can be visualized with the help of visualization tools like paraview and Vu. Note that paraview is a free visualization software, while Vu has to be purchased from invisu.ca.

Table 2.1: Description of the format and contents of the output files produced by PTetra. The six digits embedded in the file name after letter "pictetra" represent the timestep at which it was produced. In parallel processing, PTetra produces the same number of restartfiles (.rdm) as the number of processors, and the number following the underscore "_" indicates the processor id from which it was obtained.

File name	Description of the contained quantities
pictetra.hst	Physical time, species densities, collected charge and current by each structure, and their electric potential.
pictetra060500.vu	Charge density, potential, electron density and temperature, ion density, perturbed plasma current density and associated magnetic field perturbation.
scc061000.vtk	Magnitude of collected surface current density.
pictetra058612.topo	Electrostatic potential and its average. This file is used in test-particle calculations.
pictetra060339_000099.rdm	Particles positions, velocities, statistical weights. For macro particles corresponding to ions, the file also includes the charge and mass.

2.4 Test-particle modeling

Several authors have discussed and used the test-particle approach including, for example [62, 63, 64, 65, 66, 67, 68, 69, 70]. In this work, Backtracking Liouville [71, 72] is used to calculate distribution functions of ions and electrons at specific locations. The underlying assumption in this formulation is that the

plasma is well described by the Vlasov equation

$$\frac{df}{dt} = \frac{\partial f}{\partial t} + \vec{v} \cdot \frac{\partial f}{\partial \vec{r}} + \frac{q}{m}(\vec{E} + \vec{v} \times \vec{B}) \cdot \frac{\partial f}{\partial \vec{v}} = 0, \tag{2.18}$$

and therefore the single particle distribution function $f(\vec{r}, \vec{v}, t)$ is constant along a particle trajectory.

The approach can be illustrated with an example in which a square satellite is contained in a larger square simulation domain as illustrated in Fig. 2.2. In this example, let us assume that plasma is injected from the left side (the

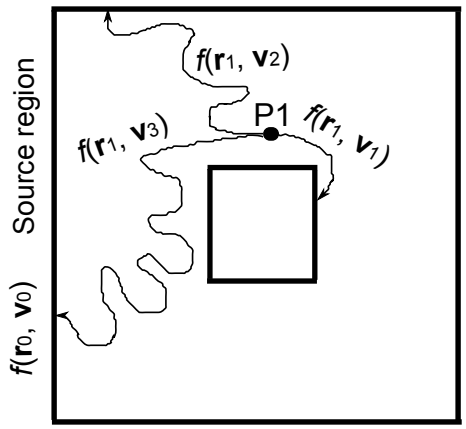

Figure 2.2: Illustration of the backward Liouville approach. A drifting Maxwellian plasma is injected from the left side of the square acting as a source region. Point $P1$ is located near a square satellite where the distribution function is to be calculated with the backward Liouville approach.

source region) of the outer boundary, where the distribution function is a known drifting Maxwellian. The Backtracking Liouville method can then be used to find the distribution function at point $P1$ where the distribution function is unknown. In this method, particle trajectories are integrated backward in time from point $P1$ using equations 2.10 and 2.11. If a backward integrated trajectory intersects the satellite or the square sides other than the left side

(source region), the corresponding distribution function is set to zero; e.g.,

$$f_{P1}(\vec{r_1}, \vec{v_1}) = f_{P1}(\vec{r_1}, \vec{v_2}) = 0. \tag{2.19}$$

If the trajectory reaches the source region, however, the numerical value of the particle distribution function at point $P1$ then becomes

$$f_{P1}(\vec{r_1}, \vec{v_3}) = f_{source}(\vec{r_0}, \vec{v_0}), \tag{2.20}$$

where f_{P1} and f_{source} are the distribution functions at point $P1$ and source region respectively. This approach is equivalent to solving the Vlasov equation. It is noteworthy to mention that in backward integration of particles trajectories, the sign of velocity and magnetic field vector must be changed in order to do the integration. An alternative to this, the Forward Liouville approach is similar except that particle trajectories are now integrated forward in time from the source region, and particle final velocities sampling is done over a finite volume element. A detailed study of both approaches is presented by Voitcu et al. in the article [73].

The advantage of using test-particle simulations with backtracking, compared to a direct calculation of particle distribution functions from PIC simulation results is that distribution functions can be obtained with essentially no statistical errors [71]. It is noted that in general, test-particle simulations are not self-consistent because computed particle trajectories are not used in the calculation of the fields used to calculate them. The general assumption is that the fields used in the integration are a good approximation to the actual fields. These can be obtained from observation or from an approximate computer model. In the present study, however, the fields are obtained from fully kinetic and self-consistent PIC simulations, and they are believed to be very good approximations of the actual fields.

Chapter 3

Sheath and magnetic field effects on Swarm electric field instrument

3.1 Introduction

This chapter is based on two published papers in peer reviewed journals [53, 54]. In this chapter, the effect of plasma-satellite interaction in the presence of Earth's magnetic field on the measurements of the electric field instrument (EFI) is studied. The EFI is carried by each of the three Swarm satellites and consists of two thermal ion imagers (TIIs), mounted on the ram face, and two spherical Langmuir probes close to the ram face, pointing in the nadir direction, as shown in Fig. 1.6 of chapter 1. The TII is designed to collect ions incident from two perpendicular planes in the ram direction and project them on a micro channel plate (MCP) consisting of a 64×64 detector array. The distribution of ion fluxes on the array provides a measure of the three-dimensional ion velocity distribution functions. Moments of these fluxes serve to determine the velocity $\vec{v}$ of the incident plasma flow in the frame of the satellite and infer local electric fields from the relation $\vec{E} = -\vec{v} \times \vec{B}$, where $\vec{B}$ is the local

magnetic field. The two Langmuir probes measure the current-voltage (I-V) characteristics and their analysis provides the measurements of in situ electron temperature and density.

In a recent article [74], Marchand et al. used a combination of PIC and test-particle techniques to simulate the electrostatic sheath on the ram face of the Swarm satellites to study its effect on ion velocity measurements made by TIIs. This study led to the finding that sheath effects could cause aberrations in the inferred plasma flow velocities of order 37 m/s or less. The study, however, was carried out without accounting for ambient magnetic field effects. In the following section, the first assessment of magnetic field effects on the Swarm' TII measurements was investigated. The calculation proceeds in three steps. First, the structure of the electrostatic sheath surrounding the spacecraft and the TIIs is calculated with PTetra. Test-particle modeling with particle backtracking is then used to compute ion distribution functions at the TII apertures. Finally, these computed distribution functions are used to track ions into the sensors, down to the MCP, from which fluxes are calculated on the 64×64 pixel array. These in turn correspond directly to what will be measured with the TIIs.

The effect of a Langmuir probe support and a simplified spacecraft (in the form of right-angled parallelepiped) on the probe collected current was investigated using the Space Plasma Interaction System (SPIS) code by Chiaretta, in his thesis [75] where a single probe without magnetic field effects was considered. In the Langmuir probes section of this chapter, a more detailed geometry containing both probes, along with their structural details, and a larger spacecraft body in the presence of Earth's magnetic field is simulated. The I-V characteristics for each of the probe are calculated with and without local magnetic field. The effect of magnetic field on the particle distribution func-

tions at the tips of probes as well as the mutual coupling between them is also investigated.

3.2 Thermal ion imagers

The goal of the present section is to study magnetic field effects on the sheath surrounding TII sensors and their measurements. Therefore, the geometry of a satellite is simplified considerably by a) truncating it to only a fraction of the ram section and b) limiting a detailed description of the geometry to the immediate vicinity of the front plate and TIIs. The geometry considered in the simulations is illustrated in Fig. 3.1. The assumption made here is that this

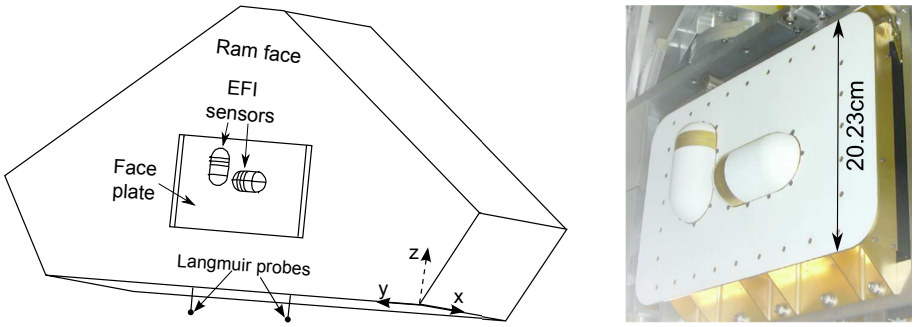

Figure 3.1: Simplified Swarm satellite geometry (left). The cylindrical TII sensors (shown on right), and Langmuir probes constitute the EFI. Each sensor entrance is flanked with two gold strips deposited on the shells. Note that while the position of the two Langmuir probes is illustrated here for reference, these probes are only included in the satellite geometry simulated in next section of this chapter.

truncated and geometrically simplified representation of the spacecraft is sufficient to describe the main effect of the electric sheath and ambient magnetic fields on TIIs. This assumption was verified with simulations that accounted for a more complete description of the spacecraft over the ~ 9 m of its length. The main effect was a decrease in the floating potential (an increase in absolute value) by $\sim 28\%$. The structure of the sheath near TIIs and its effect on particle distributions and fluxes described below were otherwise unchanged. The

numerical approach used in this study are described in chapter 2.

In this section the results from two case studies obtained with Earth's magnetic field and plasma parameters that are representative of those expected along Swarm orbits are presented. For reference and comparison purposes, one case is also carried out without magnetic field. Specifically, in all cases the background plasma assumed in the simulations consists of singly ionized oxygen and hydrogen ions with densities $n_{O^+} = 2.25 \times 10^{10}\mathrm{m}^{-3}$ and $n_{H^+} = 0.25 \times 10^{10}\mathrm{m}^{-3}$. The electron density is determined from quasi-neutrality to be $n_e = 2.5 \times 10^{10}\mathrm{m}^{-3}$. All species temperatures far from the spacecraft are assumed to be equal to $T = 0.2\mathrm{eV}$. Also all species are assumed to drift in the spacecraft reference frame, with the negative satellite orbital velocity; that is with velocity $\vec{v}_d = 7587\mathrm{m/s}\hat{x}$. Referring to Fig. 3.1, the two cases considered with magnetic field effects assume $\vec{B} = -40\mu\mathrm{T}\hat{z}$ and $\vec{B} = 40\mu\mathrm{T}\hat{z}$ expected near the geographic North and South poles respectively. By comparing results obtained in the three cases it is possible to assess the effect of the magnetic field both qualitatively and quantitatively.

3.2.1 Spacecraft floating potential and the electrostatic sheath

Spacecraft floating potential and the surrounding electrostatic sheath are computed with PTetra for the three cases mentioned above. In these simulations all species are treated fully kinetically and the code is run in time-dependent mode until a steady state is reached. In the three cases, the spacecraft floating potential, given in table 3.1, is approximately $-3kT/e$, with the least negative values found when a magnetic field is taken into account. In the presence of a magnetic field transverse to the plasma flow there exists a motional electric field $\vec{E} = -\vec{v} \times \vec{B}$, which leads to an electric potential gradient and thus varying

values of ϕ around the outer simulation boundary. As a result, a spacecraft potential depends on its position relative to the boundary, even in the absence of charging or sheath electric field [57]. The physically meaningful 'floating potential' in this case is therefore not the value of the potential computed at steady state, when no net current is collected, but rather the difference between this potential and the one computed when the spacecraft carries no charge and surrounding plasma is charge neutral. It is this difference that is reported in the table. The reduction in the absolute value of the negative floating potential with a magnetic field, is consistent with the fact that, for the parameters considered, the electron thermal gyro-radius ($\rho_e \sim$ 3cm) is smaller than the size of the spacecraft, while the ion gyro-radii ($\rho_{H^+} \sim$ 1m, $\rho_{O^+} \sim$ 4.5m) are larger. As a result, electrons are magnetized and constrained to move to the spacecraft effectively in one dimension along the field line. Ions, on the other hand, are effectively unmagnetized and can reach the spacecraft from any direction. The result is that the floating potential has to be less negative in order to repel a smaller incoming electron flux and ensure zero net collected current at steady state [57]. While the geometry considered in these simulations did not

Table 3.1: Spacecraft floating potential and potentials calculated at the tips of the Langmuir probes (mV) from three different simulations at steady state. The x and y positions of the centroids of the O^+ fluxes, defined in pixel units (see Eq. 3.1), are also given in each case. The uncertainty in the potentials is estimated to be approximately $\pm$0.5 mV.

Magnetic field (10^{-5}T)	$B = -4$	$B = 0$	$B = 4$
Floating potential	-653	-657	-653
Left Langmuir probe	-9.2	-53.8	-88.8
Right Langmuir probe	-89.1	-54.5	-8.1
$\bar{x}$	46.43	46.46	46.40
$\bar{y}$	-0.36	0.004	0.38

account for the Langmuir probes shown in Fig. 3.1, it is of interest to consider the plasma potential at their locations. The solution to Poisson's equation at steady state is used to determine the potential at the probes' tips in the three

cases considered. The resulting values are given in table 3.1. Considering the separation of 30 cm of the probes in the y direction, my calculations indicate that a reading of the potential from these positions would lead to an estimate of the electric field in the y direction $E_y \simeq -0.27\text{V/m}$ for $B = -4 \times 10^{-5}$ T and $E_y \simeq 0.27\text{V/m}$ for $B = 4 \times 10^{-5}$ T. These are close to the values expected from $\vec{E} = -\vec{v} \times \vec{B} \simeq \mp 0.30\text{V/m}\hat{y}$ corresponding to $\vec{B} = \mp 4 \times 10^{-5}\text{T}\hat{z}$. This discrepancy in the electric field is due to the proximity of the probe tips to the spacecraft body. A study of the probes' characteristics accounting for their detailed geometry is presented later in this chapter. The effect of B_z is best understood by looking at equipotentials in the $x - y$ plane. Three sets of equipotentials, corresponding to the three cases considered, are shown in Fig. 3.2. In this figure, the cross section chosen for the equipotentials is such that it goes through the aperture of the horizontal TII sensor (the one located in the direction of $+y$ in Fig. 3.1). In the absence of a magnetic and associated electric field, the equipotentials surrounding the spacecraft display an approximate mirror symmetry in the $y = 0$ plane. With a magnetic field, however, the associated $-\vec{v} \times \vec{B}$ electric field is seen to cause a significant distortion of the equipotentials in the y coordinates. With $B = -4 \times 10^{-5}\text{T}\hat{z}$, the ambient $\vec{E}$ is directed along $-y$, and equipotentials are seen to wrap around the satellite and 'pile up' on the $y > 0$ side. This in turn leads to a stronger electric field on that side of the spacecraft than on the opposite ($y < 0$) side. The opposite is observed for $B = 4 \times 10^{-5}\text{T}\hat{z}$.

3.2.2 Ion distribution functions around TII's apertures

Given the potential field surrounding the spacecraft and the TII apertures, particle backtracking is used to compute the velocity distribution functions for both ions species at 31 points uniformly distributed around each TII aperture. Each distribution function f is discretized on an unstructured block adaptive mesh in velocity space, in which more mesh points are created where f is

significant and varies appreciably. The effect of the induced $-\vec{v} \times \vec{B}$ electric field on the sheath is clearly visible in the cross sections of f shown for H^+ in Fig. 3.3. In the reference case ($B = 0$), the distribution function is seen to have approximate mirror symmetry about the $v_y = 0$ plane. The other two cases, on the other hand, show up-down asymmetries in v_y that are consistent with the shape of the equipotentials seen in Fig. 3.2. For example, 'wrapping' of equipotentials around the spacecraft from left to right (negative to positive y), leads to an electric field $-\nabla V$ with a negative y component at the horizontal aperture centre. The induced field combines with the 3-dimensional electric field in the sheath to cause this distortion. In the absence of the spacecraft, the background $-\vec{v} \times \vec{B}$ electric field would lead to a bulk $\vec{E} \times \vec{B}$ plasma drift and the distribution function would simply be a Maxwellian drifting at the negative ram velocity. The presence of the spacecraft, the fact that it is an equipotential and the resulting contouring of the equipotentials noted above, cause a strong asymmetry in the sheath in the y direction. This in turn leads to a shift of the H^+ distribution toward negative y velocities, a feature clearly visible in the left panel of Fig. 3.3. The same qualitative features are seen with $B_z = 4 \times 10^{-5}$ T, except that the asymmetry induced in the sheath by the $-\vec{v} \times \vec{B}$ field now results in a shift in the distribution function in the positive v_y direction. It is noted that the shifted distribution computed in the $v_x - v_y$ cross section, with $B_z = -40\mu$T is almost a mirror image (with respect to the $v_x = 0$ axis) of the distribution function computed with $B_z = 40\mu$T. There are in fact small deviations from exact mirror symmetry due in part to the fact that the horizontal sensor is not centred on the ram face. It is slightly to the left (toward positive y) of the centre and, as a result, when equipotentials contour the ram face from left to right as with $B_z = -4 \times 10^{-5}$ T, the sheath electric field at the centre of the horizontal aperture is slightly stronger than when contouring is from right to left. Another cause of the lack of symmetry is the proximity of the horizontal sensor aperture to the other (vertical) sensor to the right in Fig.

3.1. The results shown here are for hydrogen ions which, owing to their low mass, are most affected by sheath effects. Similar qualitative effects are found with O^+, but these are considerably smaller quantitatively due to these ions' larger mass.

3.2.3 Ion fluxes on the micro channel plate

Given the parametrisation of the particle distribution functions around the apertures, it is now straightforward to do a Monte Carlo simulation of ions injected into the sensors and compute fluxes on each pixel of the detector array. Here again, in order to minimize statistical errors, use is made of the one-particle Liouville theorem. Specifically, for each particle reaching a pixel a contribution to the flux of $v_n f$ is added, where f is the interpolated value of the distribution function computed for the injected particle and v_n is the component of the velocity particle crossing the pixel perpendicular to the MCP plane. The working principle of the TIIs is illustrated in Fig. 3.4 for reference. More details concerning this instrument can be found in [76]. Normalized fluxes computed on a 32×64 array of pixels of the horizontal sensor are shown in Fig. 3.5 for the three cases considered. For a z directed magnetic field considered here, the $-\vec{v} \times \vec{B}$ electric field is in the y direction, and it only has a significant effect in the 'horizontal' $(x - y)$ direction. For that reason, the discussion in the following is limited to the horizontal sensor only. Similar effects would be found for the vertical sensor if the ambient magnetic field were in the y direction (corresponding to $-\vec{v} \times \vec{B}$ in the z direction). Here, the centre of the pixel arrays is between rows 32 and 33 in y and only columns 33 to 64 in x are used for measuring particle fluxes. In the absence of sheath effects, or of ambient electric fields, ion fluxes on the MCP should be located halfway between rows 32 and 33 in y (let us refer to this as row 32.5) . That is, they should peak at row index 32.5, and they should display mirror symmetry in y with respect to that position. To good approximation this is what is observed in the $\vec{B} = 0$

reference case. The other two cases, with $\vec{B} = \mp 4 \times 10^{-5} \mathrm{T}\hat{z}$, on the other hand, show up-down asymmetries in the flux profiles. In particular there is a clear shift in the flux maximum toward lower row indices (lower values of y) when $\vec{B} = -4 \times 10^{-5} \mathrm{T}\hat{z}$. This shift is consistent with the shift computed in the H^+ distribution function when the ambient electric field points in the negative y direction, as shown in Fig. 3.3. The opposite is seen when $\vec{B} = 4 \times 10^{-5} \mathrm{T}\hat{z}$ and, again, it is consistent with the shift in the velocity distribution function found in this case.

It is instructive to quantify the shift introduced in the ion fluxes to the MCP by computing moments of the pixel indices for the three cases considered, since the ion flow velocity is to be determined with TIIs from these moments. Monte Carlo simulations have been made to establish a nearly linear relation between the displacement of the centroid of the O^+ flux from the centre of the pixel array, and incoming plasma flow velocity. The relation between the two is such that a shift by one pixel corresponds to a plasma velocity of approximately 600 m/s. Furthermore, laboratory testing of the TII instruments demonstrates a velocity sensitivity of 5 m/s, corresponding to a sensitivity of 0.01 pixel (D. Knudsen, personal communication). Taking the centre of the pixel array at row 32.5, the x and y positions of the centroid of the oxygen flux distribution on the MCP are calculated as

$$(\bar{x}, \bar{y}) = \sum_{i_x=i_1}^{i_2} \sum_{i_y=1}^{64} (i_x, i_y - 32.5) F(i_x, i_y) \Bigg/ \sum_{i_x=i_1}^{i_2} \sum_{i_y=1}^{64} F(i_x, i_y), \qquad (3.1)$$

where $F(i_x, i_y)$ is the flux in pixel i_x, i_y, and indices i_1 and i_2 are chosen so as to limit the calculation of the moment to that of the O^+ flux only. Thus, for the cases considered above, $i_1 \sim 42$ and $i_2 \sim 52$ are chosen. Operationally, the TII instrument detects the O^+ signal for bulk flow analysis since O^+ typically dominates other ion species at Swarm altitudes ($\sim$ 500 km), and because O^+

ions, on account of their larger mass, are less affected by the sheath than lighter ions. The pixel coordinates of the centroid $(\bar{x}, \bar{y})$ obtained in the three cases considered are given in table 3.1. Comparing these cases, it follows that magnetic fields are expected to lead to systematic and periodic (along the orbits) shifts in the pixel coordinates of approximately ± 0.37 in y. Owing to the proportionality between pixel position and velocity mentioned above, if magnetic field effects were not accounted for in the interpretation of the fluxes, there would result systematic aberrations of $\simeq \pm 200$ m/s in the y component of the plasma flow velocity. The effect in the x component of the plasma velocity is seen to be much smaller. Comparing with the reference $B = 0$ case, the x coordinates of the O^+ flux centroids calculated with $B_z = -4$, and $4 \times 10^{-5}\mathrm{T}\hat{z}$, are seen to vary by -0.03 and -0.06 respectively. This would correspond to aberrations in the x component of the velocity of $\lesssim 36$ m/s.

3.3 Langmuir probes

In this section, the two EFI Langmuir probe characteristics are simulated under representative ionospheric conditions with, and without a magnetic field. For simplicity, only a short section ($\sim$ 1 m) of the ram end of the satellite is considered. All components of the satellite are assumed to be equipotential, except for the sections of the Langmuir probes' support, which are all assumed to be floating. In the simulations, the spherical tip of the probes bias with respect to the payload is set as an input parameter. These conditions are only approximate as different parts of the satellite (e.g., the front plate supporting the TII sensors or the tips of the Langmuir probes) will be biased with respect to one another. Potential differences will also exist between surfaces made of materials with different work functions [77]. The geometry considered in the simulations is illustrated in Fig. 3.6. The coordinates are such that x points in direction of the plasma flow as seen in the satellite rest frame, z points in

the zenith direction, and y is such that x, y, z is right handed. The geometry of the two Langmuir probes (shown in Fig. 3.6) positioned at the base of the ram end of Swarm is as described in Chiaretta's recent thesis [75].

3.3.1 Sheath and ion distribution functions around Langmuir probes in presence of geomagnetic field

The spacecraft floating potentials without and with magnetic field are found to be the same as given in table 3.1; that is $V_f = -0.657$ V and $V_f = -0.653$ V with $\vec{B} = 0$ and $\vec{B} = -40\mu\mathrm{T}\hat{z}$ respectively. The effect of $\vec{B}$ is clearly illustrated by comparing equipotentials computed near the probes. Figure 3.7 shows equipotentials in the $y-z$ plane intersecting the center of the Langmuir probes. In this simulation, all components of the probes (including the spherical tip) were assumed to be independently floating. With the neglect of $\vec{B}$, equipotentials are nearly symmetrical between the left and right probes. With $\vec{B} = -40\mu\mathrm{T}\hat{z}$, however, the background $-\vec{v}\times\vec{B}$ electric field is seen to cause a significant distortion in the equipotential lines and thus breaks that symmetry. As a result, with the direction of the magnetic field considered and with the assumed boundary conditions, the potential of the left probe is higher than that on the right by approximately 80 mV. This potential difference is less than the 91 mV expected from the $-\vec{v}\times\vec{B}$ background electric field and the 30 cm separating the two probes along y. The discrepancy is due to the proximity of the probe tips to the other components of the probes, to the (grounded) payload and to the (mutual) capacitive coupling between these components.

Another comparison showing the effect of the magnetic field is with the particle distribution function at the lower tip (in z) of the Langmuir probes. Figure 3.8 shows a cross section of the velocity space H^+ distribution f_{H^+} in the $v_x - v_y$ plane computed at the tip of the right probe. The distribution function

was obtained at that position with minimal statistical noise, using test-particle back tracking [71]. The figure shows a significant change in the distribution f_{H^+} caused by the magnetic field. Similar results have been found for f_{H^+} at the tip of the left probe, and for the oxygen ion distribution functions. Sheath effects on O^+ ions are qualitatively similar but significantly smaller quantitatively, owing to O^+ ions' larger mass and kinetic energy.

3.3.2 Probe characteristics and mutual coupling

PTetra was used to calculate the characteristics of the Langmuir probes in order to assess: i) the mutual coupling between the two probes and ii) the effect of the magnetic field. Figure 3.9 shows the characteristic computed for the left probe in Fig. 3.6. In the simulations, except for the probe tips, the various components of the probe support were assumed to be independently floating. Unless stated otherwise, all characteristics are computed assuming the same bias voltage on both probes, with respect to the payload. The characteristic calculated for the right probe is essentially the same as for the left one, and it is not shown here. In the figure, error bars indicate uncertainties estimated from the standard deviations in the fluctuations of the collected current calculated at steady state. In the range of voltages considered, the electron ($V > 0$) and ion ($V \leq 0$) currents are seen to be linear functions of the bias voltage. A cross section of the potential in the plane containing the probes is shown in Fig. 3.10. It is interesting to note that, despite the fact that the sheath surrounding the probes is only larger than the probe radius by a factor ~ 2, this linear dependence is consistent with orbital motion limited (OML) theory, which predicts $I \simeq I_e(1 + e\phi/T_e)$ for $V > 0$, and $I \simeq I_i(1 - e\phi/T_i)$ for $V < 0$ [78]. The solid lines in the figure show least square fits computed from simulated characteristics, assuming the linear dependences between I and V mentioned above. The mutual influence or 'crosstalk' between Langmuir probes is assessed by com-

paring the collected currents when both probes are at the same bias voltage (circles in Fig. 3.9) with that when they have opposite biases (squares). The effect is found to be negligible up to the highest voltages considered here; that is, the current collected by the right probe when it is biased at ± 5 V is the same whether the left probe has the same (± 5 V) or the opposite (∓ 5 V) bias (Fig. 3.10). This shows that crosstalk between the two probes should be negligible under normal operational conditions.

The effect of the magnetic field is shown in Fig. 3.11, which compares collected currents computed with (circles) and without (triangles) magnetic field. The magnetic field assumed here is the same as in the previous cases: $B_z = -40\mu$T. Owing to the large ions gyro-radii (mentioned in the previous section), ions are effectively unmagnetized, and the characteristics computed with or without magnetic field are essentially the same when ion current is collected ($V < 0$). The collected electron current ($V > 0$) characteristic, however, has a larger slope when calculated without magnetic field. This may be unexpected considering the fact that the thermal electron gyro-radius $\rho_e \sim 3$ cm is larger than the probe radius ($a \simeq 3.8$ mm) by a factor ~ 7. The discrepancy comes from the fact that, while weakly magnetized, electrons that are collected by a probe must come from a flux tube of radius of order ρ_e. This constraint on the electrons that can be collected by the probes is associated with the fact that electrons predominantly gyrate along magnetic field lines with a gyro-radius typically equal to their thermal Larmor radius. As a result, probe tips can only collect electrons within a cylinder of radius of order two thermal electron Larmor radii. On the other hand, when $B = 0$, collected electrons can come from a broader region of space. The restriction on the volume from which electrons can be collected in the presence of a magnetic field, results in a smaller collected current for a given positive bias voltage, than when no magnetic field is present.

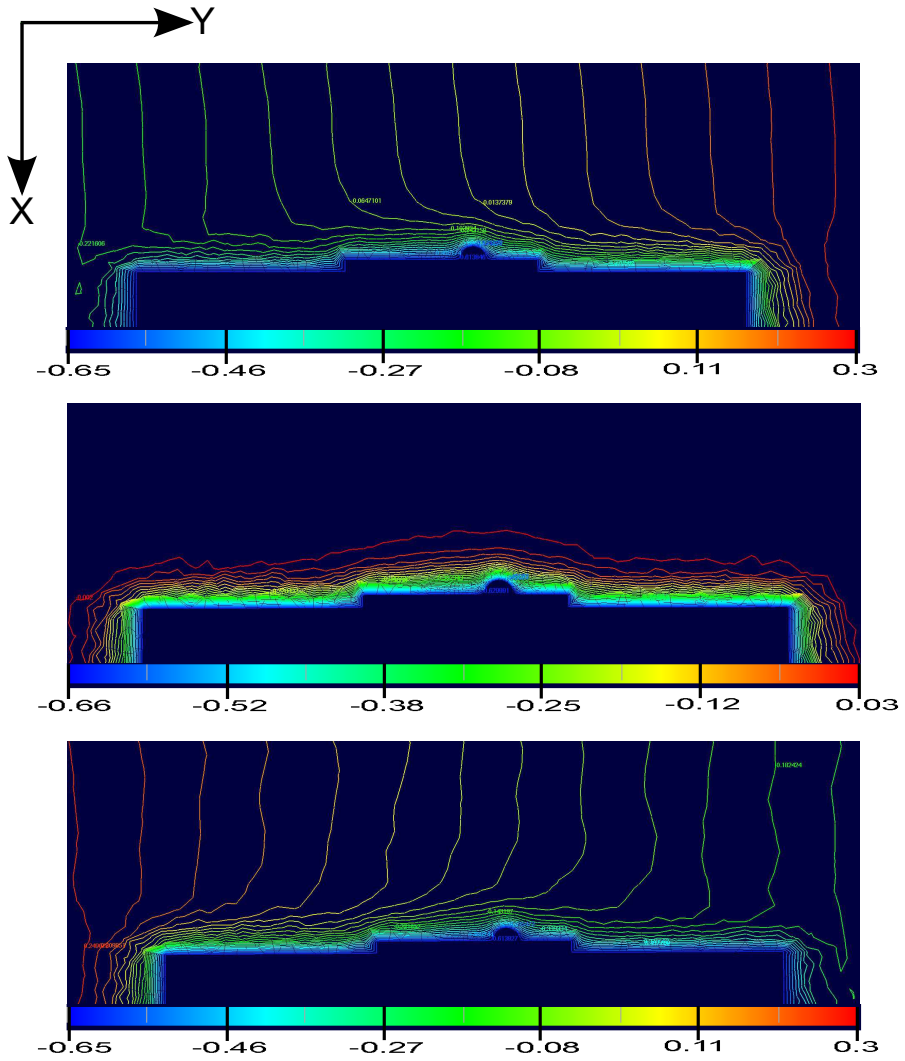

Figure 3.2: Equipotential contours computed with $B = -4 \times 10^{-5}$ T (top), $B = 0$ T (middle), $B = 4 \times 10^{-5}$ T (bottom). The numbers along the color bars give the values of the electric potential in volts.

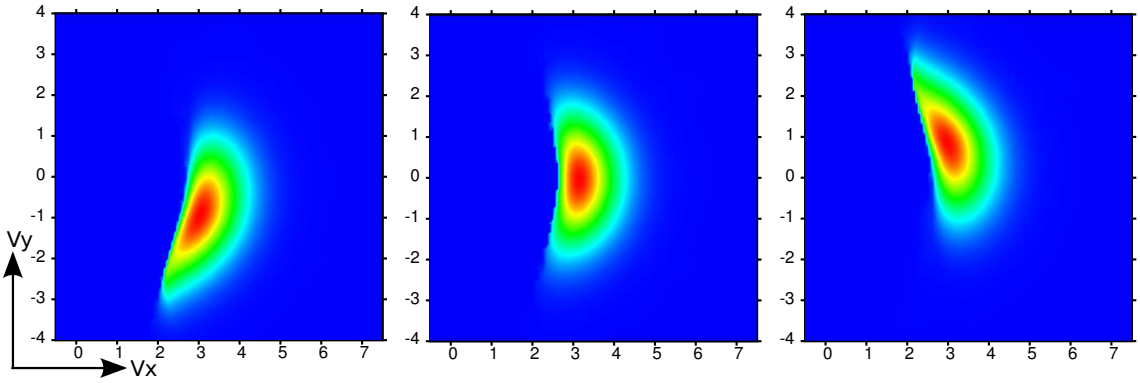

Figure 3.3: Hydrogen ion distribution function at the central point of the horizontal TII sensor aperture for $B = -4 \times 10^{-5}$ T (left), $B = 0$ T (centre), $B = 4 \times 10^{-5}$ T (right). The numbers along the axes represent the velocities of hydrogen ions, normalized by its thermal velocity ($\sqrt{T/m_{H^+}}$).

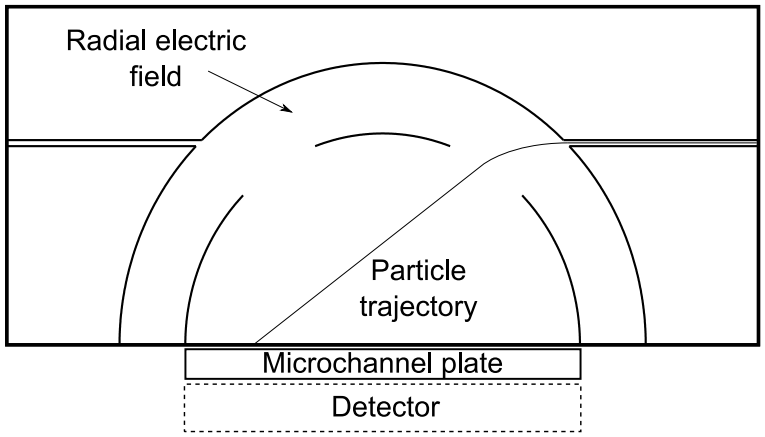

Figure 3.4: Cross section of a TII showing an example particle trajectory penetrating through the tunnel, being deflected by the radial field generated between two concentric hemispheres and precipitating on the MCP. The potential difference between the two hemispheres is 60 V.

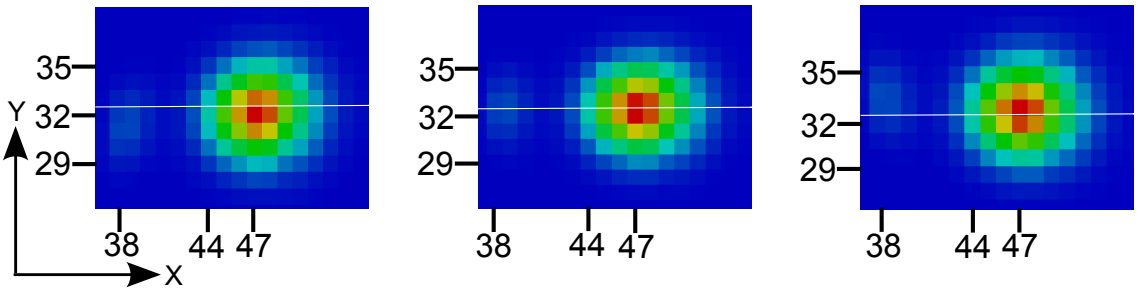

Figure 3.5: Normalized ions fluxes computed on the 32×64 array of horizontal MCP sensor in the $z = 0$ plane for $B = -4 \times 10^{-5}$ T (left), $B = 0$ T (middle), $B = 4 \times 10^{-5}$ T (right). Tick marks along the axes represents the number of pixels on the MCP. The largest flux is from the majority oxygen ions, whereas the lower flux on the left (x-pixel index $\sim$ 38) is from the minority (10%) hydrogen ions. The horizontal white line in the figures indicates the boundary between rows 32 and 33. It is the centre of the pixel array in the y direction.

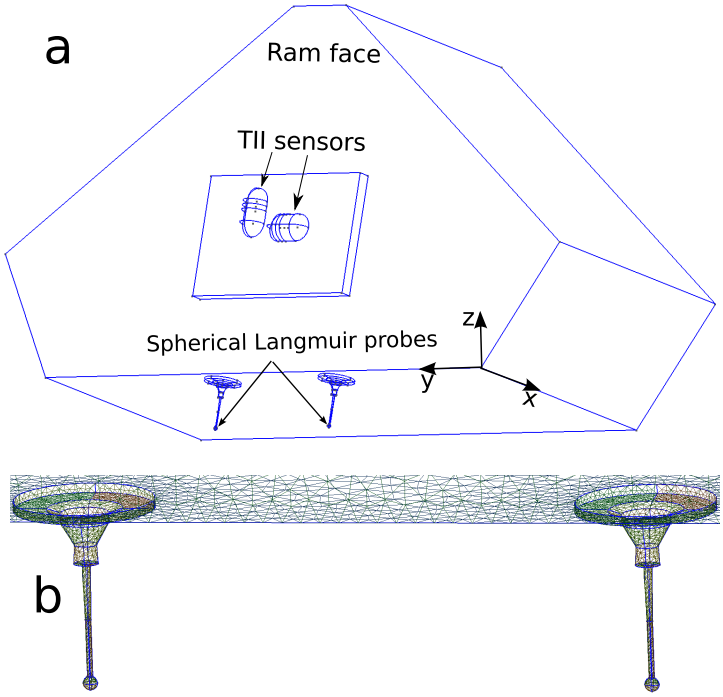

Figure 3.6: Illustration of the truncated Swarm geometry with TII sensors mounted on a face plate, and the two Langmuir probes. The lower panel (b) shows a magnified view of the Langmuir probe geometry considered in the simulations.

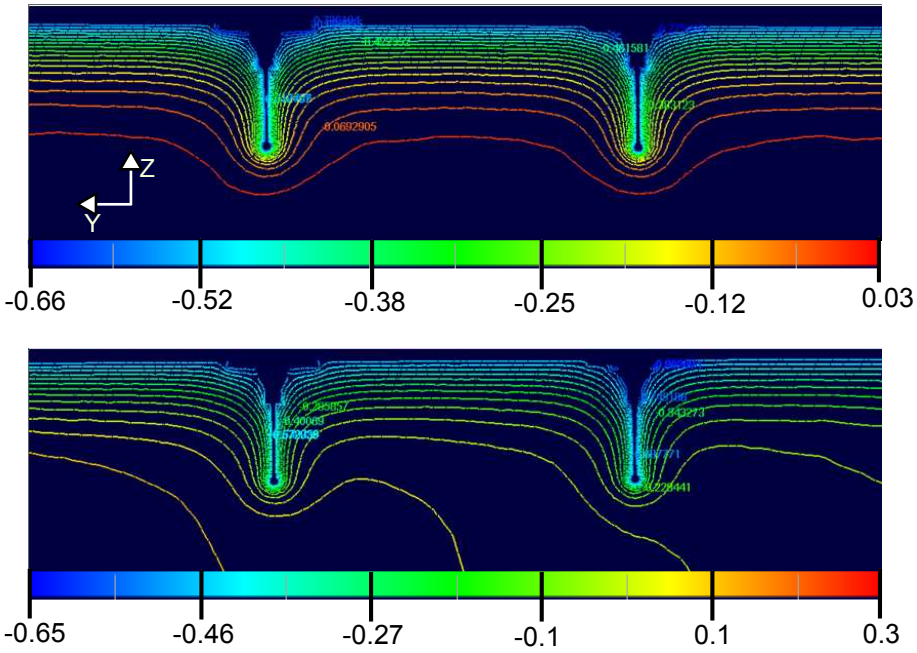

Figure 3.7: Lines of equipotential in a $y-z$ cross section computed with $\vec{B}=0$ (top) and $\vec{B}=-40\mu\mathrm{T}\hat{z}$ (bottom). Equipotentials are shown in a plane intersecting the two Langmuir probes. The color bar gives the potential in volts.

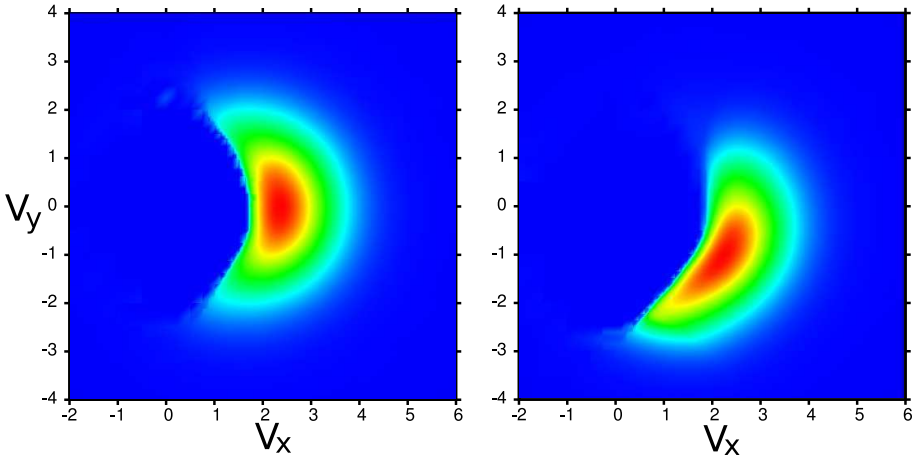

Figure 3.8: Profile of the H^+ distribution function in a v_x-v_y plane in velocity space computed without (left) and with (right) a magnetic field. Velocities are normalized with respect to the thermal velocity $v_{th}=\sqrt{T/m_{H^+}}$. In both cases, the cross section selected corresponds to $v_z=0.7v_{th}$, which contains the maximum of the distribution function.

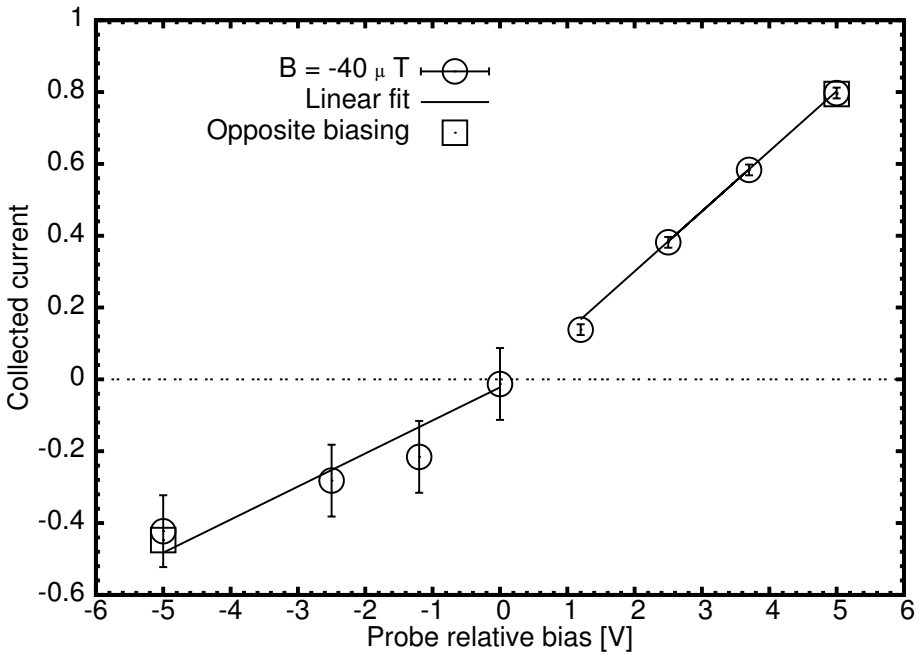

Figure 3.9: Characteristic of the left probe shown in Fig. 3.6. The units of the collected currents are μA for $V > 0$ and 10^{-8} A for $V \leq 0$. Circles refer to the characteristic computed when both probes have the same bias with respect to the payload. The squares correspond to opposite biases (i.e., ± 5 V on the right and ∓ 5 V on the left probe). Error bars indicate the uncertainties in the collected currents, based on the standard deviations calculated at steady state.

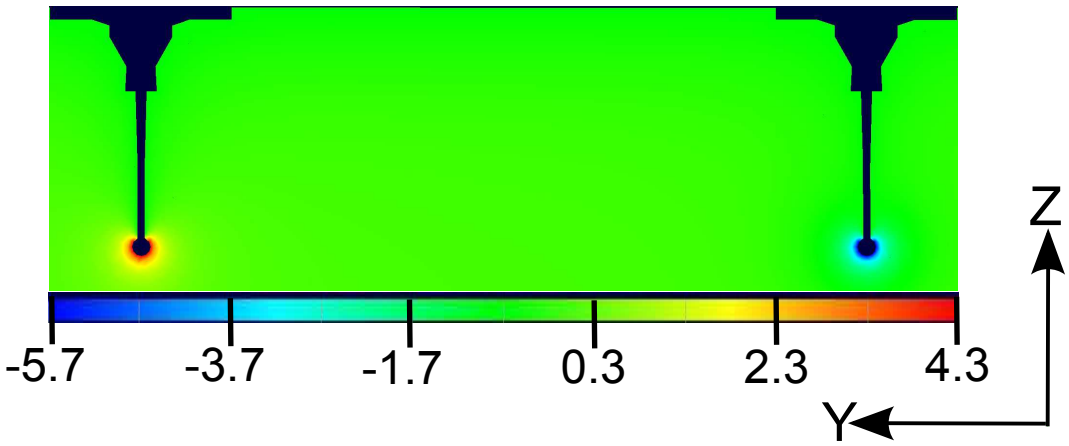

Figure 3.10: Cross section illustrating the electric potential in a plane intersecting the two Langmuir probe axes when the left and right probes are biased respectively to $+5$ V and -5 V with respect to the spacecraft. The perturbed voltages are seen to be localized in small regions surrounding the tips of the probes, which is consistent with the absence of mutual coupling between the two probes.

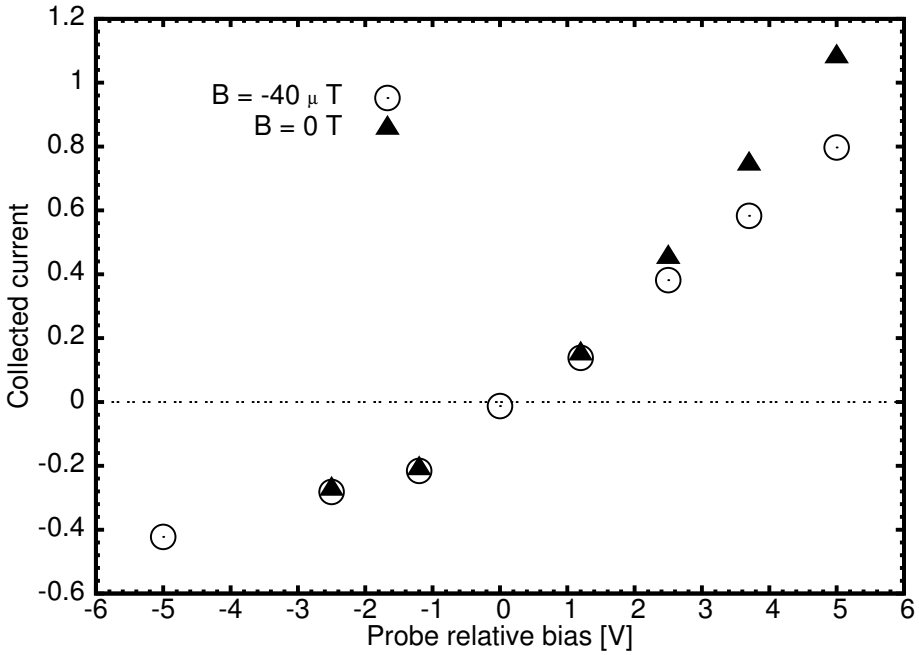

Figure 3.11: Comparison between characteristics computed with (circles) and without (triangles) magnetic field. The uncertainties in the calculated currents and the scales for the collected currents are the same as in Fig. 3.9.

Chapter 4

Magnetic field perturbations induced by plasma-satellite interaction

4.1 Introduction

The work presented in this chapter is based on a recently published letter in Physics of Plasmas [55]. The physics of electric probe interaction with plasma has been studied for nearly one century [7, 8, 79]. Since the launch of the first artificial satellite, this field of research has been extended to better understand charging of spacecraft and the electric sheaths surrounding them in the space environment [1, 2, 3, 4, 5, 6]. Our understanding of the interaction between satellites and space environment now rests on an extensive set of in situ observation, empirical knowledge, and computer simulations. In recent years, several computer models have been developed to simulate the effects of space environment on satellites, and the perturbations in this environment generated by the presence of satellites [80, 30, 81, 82, 83, 84, 85, 57]. These models serve to better understand the conditions prevailing in the environment of satellites and their effects on their instruments under given space weather conditions.

So far, these studies have been essentially limited to the electric potential and the associated field in the vicinity of spacecraft. To the author's knowledge, magnetic field perturbations associated with plasma currents induced near a spacecraft, or with closing currents in the spacecraft itself have never been measured or simulated fully kinetically. Such perturbations are almost universally deemed to be negligible and they are generally ignored in the design and operation of spacecraft instruments. This paradigm, however, is likely to change with forthcoming space missions involving increasingly sensitive instruments, operating under more extreme conditions. This is illustrated here, with the first simulation results of perturbed magnetic fields caused by spacecraft-environment interaction near the recently launched Swarm satellites. Swarm provides an interesting case study because of the unprecedented accuracy with which it will map geomagnetic fields and because of the adverse effect that field perturbations would have on these measurements if they approached or exceeded the sensitivity threshold of the magnetometers.

4.2 Problem definition

The space environment conditions selected in the analysis correspond to a satellite going over the North magnetic pole, where satellite-induced magnetic field perturbations are expected to be large, and where sudden variations in these perturbations should occur when the satellite crosses the terminator. The plasma density and temperature assumed in the simulations are $n_e = n_i = 2.25 \times 10^{10} \mathrm{m}^{-3}$ and $T_e = T_i = 0.2$ eV, with ions consisting of 90% O^+ and 10% H^+. The background geomagnetic field is assumed to be $\vec{B} = -40\mu\mathrm{T}\hat{z}$ and the plasma flow velocity in the satellite rest frame is $\vec{v} = 7587\mathrm{m/s}\ \hat{x}$. That is, the magnetic field points exactly in the nadir direction, and plasma flow is in the anti-ram direction. A simplified satellite geometry was used as illustrated

in Fig. 4.1, with fine structures omitted on the ram face and main spacecraft body. This geometry nonetheless accounts for the full length ($\sim$ 9.2 m) of

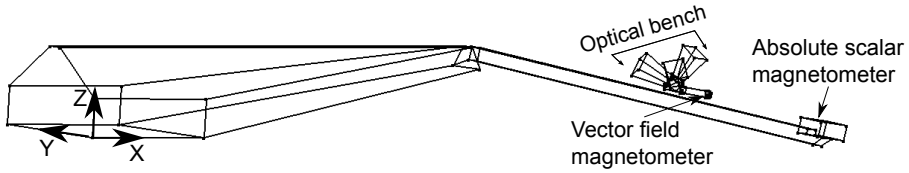

Figure 4.1: Simplified Swarm geometry used in the simulations. Detailed components are omitted from the ram side, but more details are included along the boom, where the vector and scalar magnetometers are located. The total length of the spacecraft is approximately 9.2 m.

the satellite, and for the main structures along the boom (in the wake region) where the vector and scalar magnetometers are located.

For the purpose of this study, PTetra [57], the electrostatic spacecraft-plasma interaction model, was modified to calculate first order perturbations in the magnetic field directly from kinetically computed current densities. A detailed description of the numerical approach used in PTetra was given in chapter 2. While the calculation of the perturbed electric fields are fully self-consistent, those of the perturbed magnetic field are only treated perturbatively to first order. Specifically, the magnitude of magnetic field perturbations is assumed to be much smaller than that of the background magnetic field. If this assumption can be verified a posteriori, then the neglect of perturbed magnetic field on particle trajectories is justified, and the first order estimate of perturbed magnetic fields made here is valid.

To this end, fully kinetic simulations of the interaction between the satellite and space environment were carried out for selected directions of solar irradiation, as well as for night time conditions. In each case considered, PTetra is run until a steady state solution is obtained. The current density is then calculated in each simulation cell from weighted moments of particle velocity

distributions. The resulting current density is then used to compute the perturbed magnetic field at every vertex in the simulation domain. In addition to the plasma current density, the electric current flowing along the spacecraft is also taken into account. For simplicity and for the purpose of this estimate, the current carried by the spacecraft is assumed to be in a thin wire running along the center of the main spacecraft body up to the boom, and along the boom central axis. This current is calculated as a function of x (the ram direction) by subdividing the satellite into 200 uniformly spaced bins in x, and integrating the current collected per unit surface successively over all bins. Given the current along the satellite axis, the associated perturbed magnetic field is calculated everywhere in the simulation grid, from a straightforward application of the Biot-Savart law. It is then superposed to the magnetic field computed from the plasma current density mentioned above, to yield the total perturbed magnetic field. The procedure used to account for the contribution to the perturbed magnetic field from surface and internal satellite currents, is only approximate. It is nonetheless sufficient to estimate the importance of these currents in the calculation of the total perturbed magnetic field.

4.3 Surface current asymmetry

Satellites tend to collect positive current on their ram face and negative current in the wake region to ensure a zero net collected current at steady state. For example, Fig. 4.2 shows the distribution of collected current per unit area with and without a magnetic field at night time and when solar illumination is from the $-X$ (ram) direction. As expected, the ram face collects mostly positive current, while negative current is collected on the sides and on the surfaces facing the wake.

Due to the convective potential gradient in the satellite frame of reference,

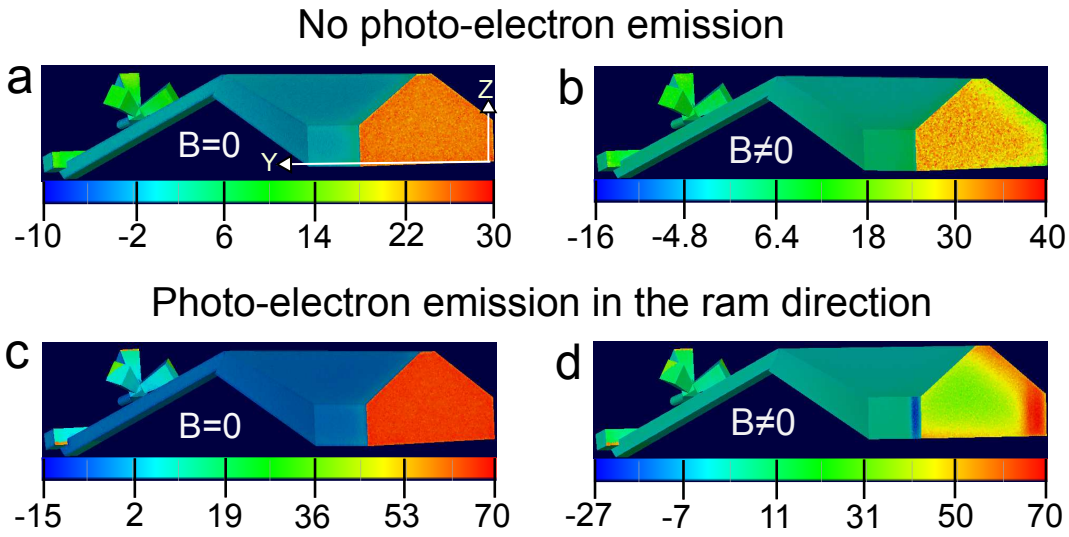

Figure 4.2: Computed collected surface current density (μAm^{-2}) at night time (panels a and b) and when solar illumination is from the ram direction (panels c and d) with (panels b and d) and without (panels a and c) the magnetic field.

the electrostatic sheath potential is stronger on the left (in $+y$ direction) side and weaker on the right side. Therefore, the left side of the ram face collects more positive current than the right side as obvious in panel (b) of Fig. 4.2.

In the presence of photo-emission from the ram side, the collected surface currents are more positive on the ram face and more negative on the side surfaces, as apparent in panel (c) of Fig. 4.2. Note that photo-electron emission contributes to positive collected current, while photo-electron redeposition associated with their relatively short gyro-radius ($\sim$ 10 cm) contributes to negative current. The current profile seen in panel (d) of Fig. 4.2 results from several processes, including photo-emission, gyration of photo-electrons in the local magnetic field, collection of background plasma particles, and the motional electric field $\vec{E} = -\vec{v} \times \vec{B}$, where $\vec{v}$ is the plasma flow velocity in the satellite frame of reference. These explain the surface current asymmetry in which the right side collects more positive current although the sheath field is weaker there; also, a strip of negative collected current on the left side is noticeable. The emitted photo-electrons from the ram side gyrate clockwise

along negative z directed magnetic field lines. The red band to the right of the ram face in panel (d) of Fig. 4.2 corresponds to the region where only photo-electrons are emitted from the ram face whereas to the left of that band, both photo-electrons emission and redeposition are occurring thus corresponding to a lower net collected current per unit area on the green band. The blue color strip on the left flank indicates a relatively large negative net collected current per unit area. This is associated with redeposition of photo-electron emitted from the left end of the ram face. It is interesting to note that in this configuration, positive current is collected by part of the optical bench and scalar magnetometer. This is due to photo-emission and the fact that these structures are not completely shadowed by the main spacecraft body.

The collected currents result in complicated current patterns in conducting surfaces, as well as inside the spacecraft body. These current distributions cannot be determined accurately without a full knowledge of the conductivity of the various surface and internal components of the satellites. In this study, a simplified model, which is described in the previous section, is used to approximate these currents and associated magnetic field perturbations. The estimated circulating surface current profiles are shown in Fig. 4.3 for a satellite without photo-electron emission (No PE) and with photo-electrons, assuming four directions of solar illumination. These correspond to illumination directly from the ram direction (PE in -X), the wake direction (PE in X) and $\pm Y$ directions (respectively PE in +Y and PE in -Y). It is noted that as expected, the integrated current at the end of the boom is zero in all cases, since at steady state, the spacecraft must collect zero net current. The largest currents are found in the wider, main satellite body owing to this component's large surface area. The narrow boom collects relatively little current, except for solar illumination from the $+X$ direction, which causes a significant positive collected current in the interval $x \in (7, 7.5)$m associated with photo-emission from the

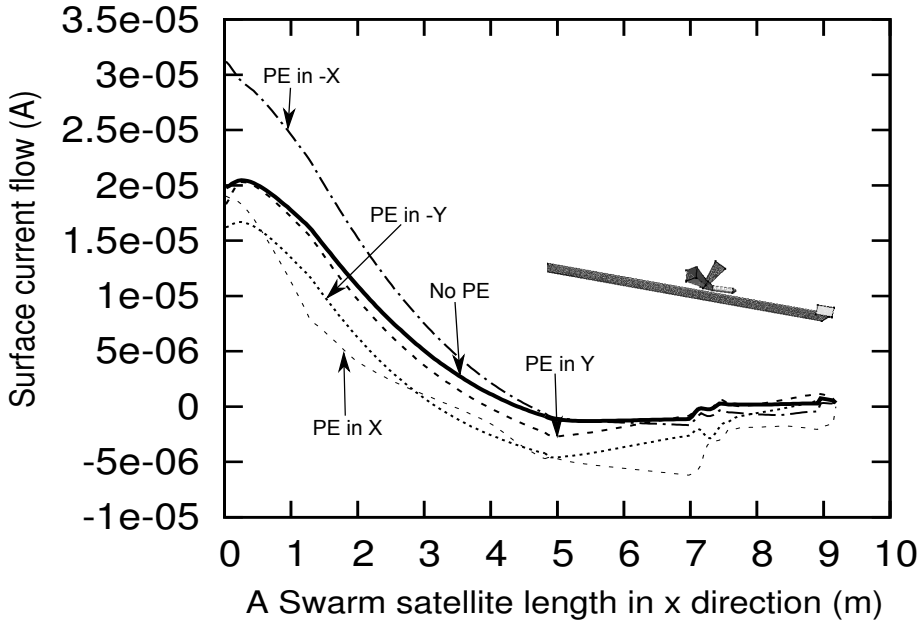

Figure 4.3: Electric current flow along Swarm for selected day and night conditions. During day time, photo-emission (PE) from the surfaces in $\pm x$ and $\pm y$ directions are considered. The approximate positions of the boom and magnetometers are also shown.

optical bench assembly.

4.4 Induced current density and perturbed magnetic field

In all simulated cases, the largest perturbed magnetic fields are found to occur near the ram face where induced plasma currents are also the largest. They range in magnitude between ~ 10 and ~ 20 pT. Figure 4.4 shows the magnitude and selected components of $\delta\vec{B}$ and $\delta\vec{J}$ obtained when solar illumination is on the ram face (from the -X direction). Induced currents and perturbed magnetic fields are seen to extend along vertical bands along the background magnetic field. The largest perturbations occur at the ram face, where the induced currents are largest. Weaker perturbations are also visible downstream along the boom, with the largest ones occurring near the optical bench and the

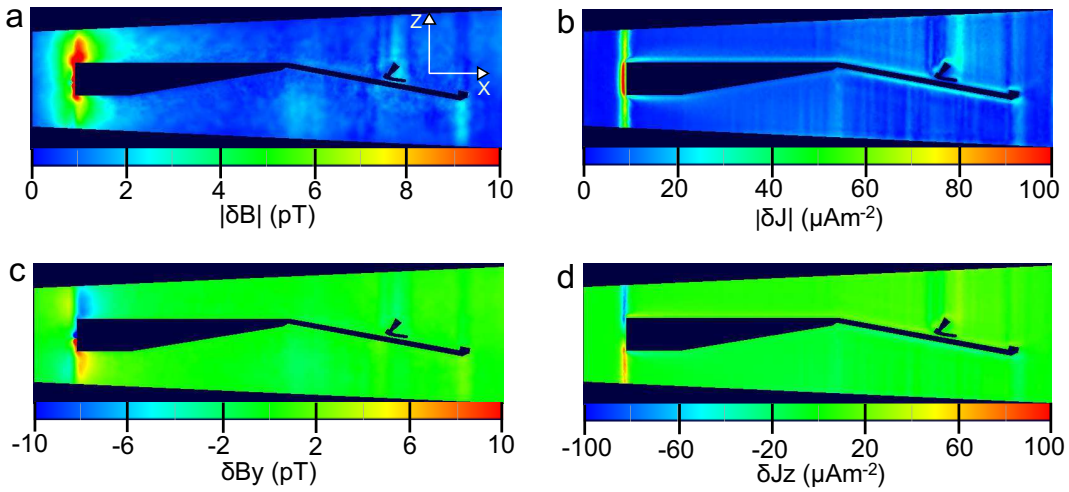

Figure 4.4: Cross section of the perturbed magnetic field (left) and the induced current density (right). The top panels (a and b) show the absolute values $|\delta\vec{B}|$ and $|\delta\vec{J}|$. The lower panels (c and d) show respectively the y component of $\delta\vec{B}$ and the z component of $\delta\vec{J}$.

scalar magnetometer. It is conspicuous that the spatial structure of magnetic field perturbations found here is qualitatively different from that of electric field perturbations found in the sheath. Indeed except for the wake region, where electric perturbations can extend over distances exceeding the length of a satellite, electric perturbations surrounding a spacecraft tend to be localized near the spacecraft due to Debye shielding [5]. Here, however, induced current densities are not shielded, they extend far from the spacecraft along field lines, and there are no visible perturbations associated with the wake.

The filamentary structure of the perturbed plasma current density and associated perturbed magnetic field can be understood as follows: a) current is mostly carried by electrons, b) in the simulations the unperturbed magnetic field $\vec{B}$ is vertical (along $\hat{z}$), and c) both thermal and photo-electrons are magnetized and constrained to move along drifting flux tubes of sizes of order one gyro-radius. The thermal electron gyro-radius is ~ 3 cm, while the average photo-electron gyro-radius is ~ 10 cm. Owing to the relatively small

drift velocity compared with the electron thermal velocities of background and photo-electrons ($\sim 1.9 \times 10^5$ and $\sim 7.3 \times 10^5$ m/s respectively), electrons are practically constrained to move along vertical flux tubes. As a consequence, photo-electrons emitted on the ram face, as well as lower energy thermal electrons $\vec{E} \times \vec{B}$ drifting toward the ram face of the satellite and being repelled by the negative spacecraft potential, can only escape along the background magnetic field, thus forming narrow vertical current channels clearly visible in panel d of Fig. 4.4. Photo-electrons emitted, or thermal electrons approaching the ram face must escape mostly in the $+z$ direction above the spacecraft and in the $-z$ direction below it. This explains the narrow band of positive and negative δJ_z respectively above and below the ram face seen in Fig. 4.4. The profile of δB_y shown in panel c can be understood from this profile of δJ_z and a straightforward application of Ampère's law. It is important to note that there is no mechanism to shield these field aligned currents, as would be the case with Debye shielding of electric perturbations. This explains why current filaments extend far from the spacecraft, up to the simulation boundary. These currents would eventually diffuse into the background plasma and close with other current filaments coming from the spacecraft. This closure, however, is not accounted for in the simulations, as it would take place over a much larger volume than is accounted for in the model.

Now turning to the perturbed magnetic field in the vicinity of the magnetometers, table 4.1 summarizes the findings for the five cases mentioned above. The computed perturbed magnetic fields are all below the $\sim$ 50pT sensitivity of the magnetometers, and should therefore be of no concern on Swarm. It is noted that, while the current carried by the spacecraft is taken into account in all the calculations, its effect on the perturbed magnetic field near the magnetometers is always relatively small. Thus, in this case, good estimates of the perturbed magnetic field can be obtained from the plasma current densities

Table 4.1: Spacecraft-plasma interaction induced perturbed magnetic fields (pT) at Swarm magnetometers for the five solar illumination configurations considered.

Solar radiation	vector		scalar
	$\delta\vec{B}$	$\lvert\delta\vec{B}\rvert$	$\lvert\delta\vec{B}\rvert$
night time	$(0.07, -0.12, -0.16)$	0.21	0.19
from -X	$(0.78, -1.01, -1.79)$	2.20	0.74
from +X	$(-0.02, -1.00, -1.00)$	1.41	0.91
from -Y	$(2.51, -2.84, -1.89)$	4.24	1.17
from +Y	$(0.03, -0.49, 1.91)$	1.97	1.41

only.

Selected cross sections of the perturbed magnetic field and current density in the boom region are shown in Fig. 4.5, for solar illumination on the ram face. This configuration is the one under which the net collected current on the ram face is strongest, as seen in Fig. 4.3. It is relevant to the crossing of the terminator during certain orbit epochs when there should be sudden variations in the induced currents and perturbed magnetic fields. The resulting small but systematic variation in $\delta\vec{B}$ in a short time period might be detectable from averages over several similar passages through the terminator. The top panels show the magnitude of the perturbed magnetic field $|\delta\vec{B}|$ in the vicinity of the magnetometers at night (left) and when solar illumination is on the ram face (right). The perturbed magnetic field computed without photo-electron emission is much smaller than that with photo-emission from the ram face. Thus, the difference between the two can be approximated simply by the latter. The middle panels of Fig. 4.5 show the amplitude of the main components of $\delta\vec{B}$ in this case. The bottom panels show the amplitude of the main components of the corresponding plasma current density δJ_z and δJ_x in two different cross sections of the simulation domain. Comparing with Fig. 4.4, the perturbed fields here are seen to be smaller than the ones near the ram face by approxi-

mately a factor 10.

In this study, the sun was treated as a point source, and in the presence of photo-emission from the ram face, the assumed satellite attitude was such that the sun was in the direction exactly perpendicular to the ram face. With the assumed geometry, this led to a small but finite exposure of the optical bench and scalar magnetometer units to solar radiation, which induced currents in the surrounding plasma and in the satellite itself. The finite width of the solar disk ($\sim 0.5^{\circ}$) and small errors in the satellites' attitude control, however, will cause a varying exposure of these structures to solar UV, thus leading to variations in the induced currents and perturbed fields near the magnetometers. This may have implications, particularly in statistical studies with Swarm data involving averages over many orbits. In such cases, if the signals considered are in the range of several pico-Tesla, satellite-environment effects should be looked at more carefully, and possibly taken into account in the interpretation of these averages.

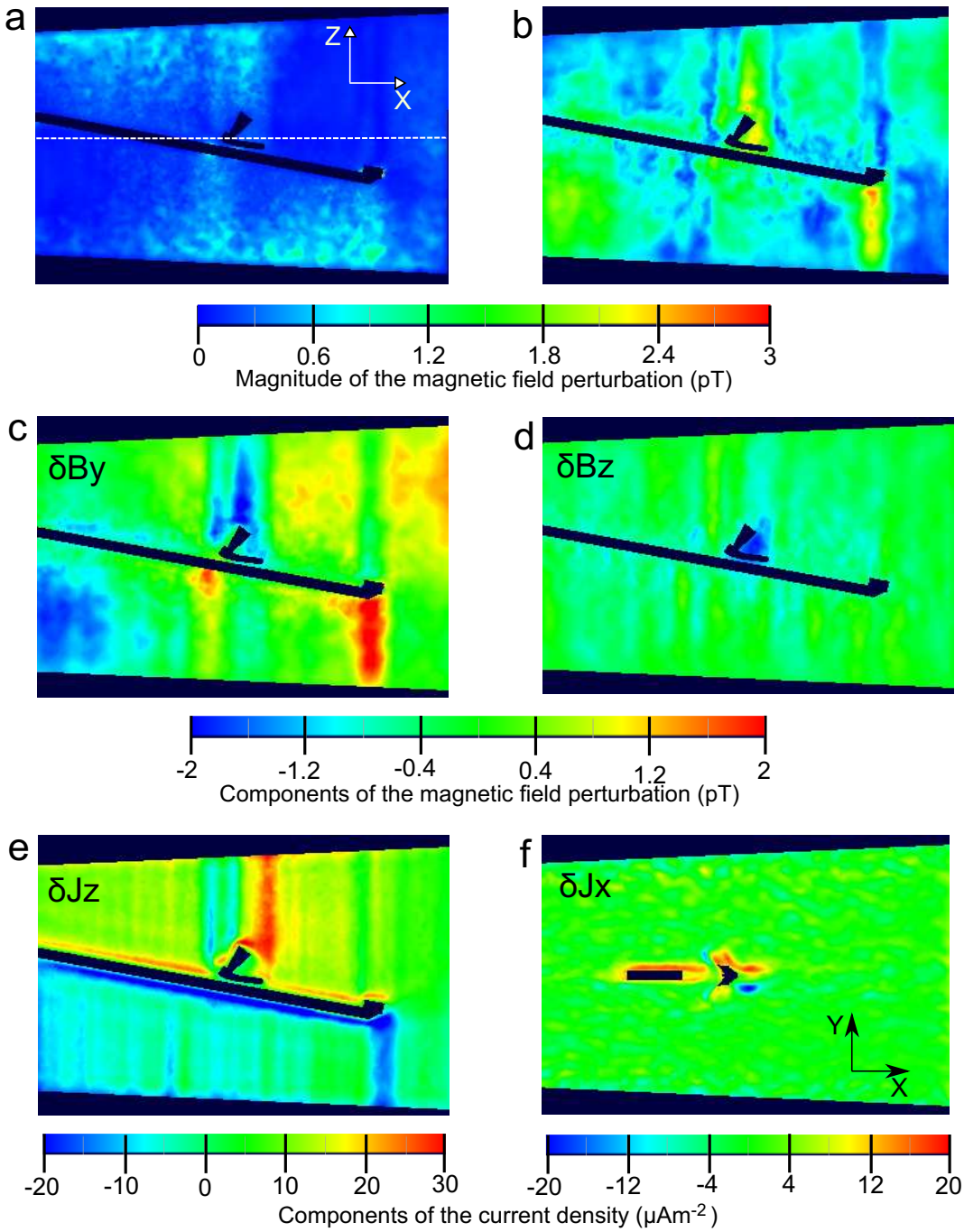

Figure 4.5: Magnitude of the magnetic field perturbation during night time, when there is no photo-electron emission (panel a) and during day time when solar illumination is on the ram side (panel b). The dominant components (δB_y and δB_z) of the perturbation are shown in panels c and d. The main components of the current density (δJ_z and δJ_x), responsible for the generation of the perturbed field are shown in panels e and f. The xy cross section in panel f intersects the z axis along the white dotted line shown in panel a.

Chapter 5

Modeling probe characteristics in a controlled laboratory plasma

5.1 Introduction

In this chapter, I compare simulation results for Langmuir probe characteristics, with measurements made in a well controlled laboratory plasma. The experiment was conducted at the ELEPHANT facility as part of a PhD project by Lisa E. Gayetsky under the supervision of professor Kristina A. Lynch in the Department of Physics and Astronomy, Dartmouth College, Hanover, New Hampshire, USA. In this experiment, an argon plasma is injected in a cylindrical vacuum chamber through 21 bore holes each of radius 1.9 mm. After being injected, the plasma expands radially to form a beam that then extends over the full length, $\sim$ 1.5 m, of the vacuum chamber. The chamber contained a conducting sphere located near the cylinder axis, approximately 50 cm from the plasma injection region, as illustrated in Fig. 5.1. In addition, as shown in Fig. 5.1, two movable Langmuir probes mounted on a spin table, were used to measure current-voltage (I-V) characteristics at different locations near the sphere.

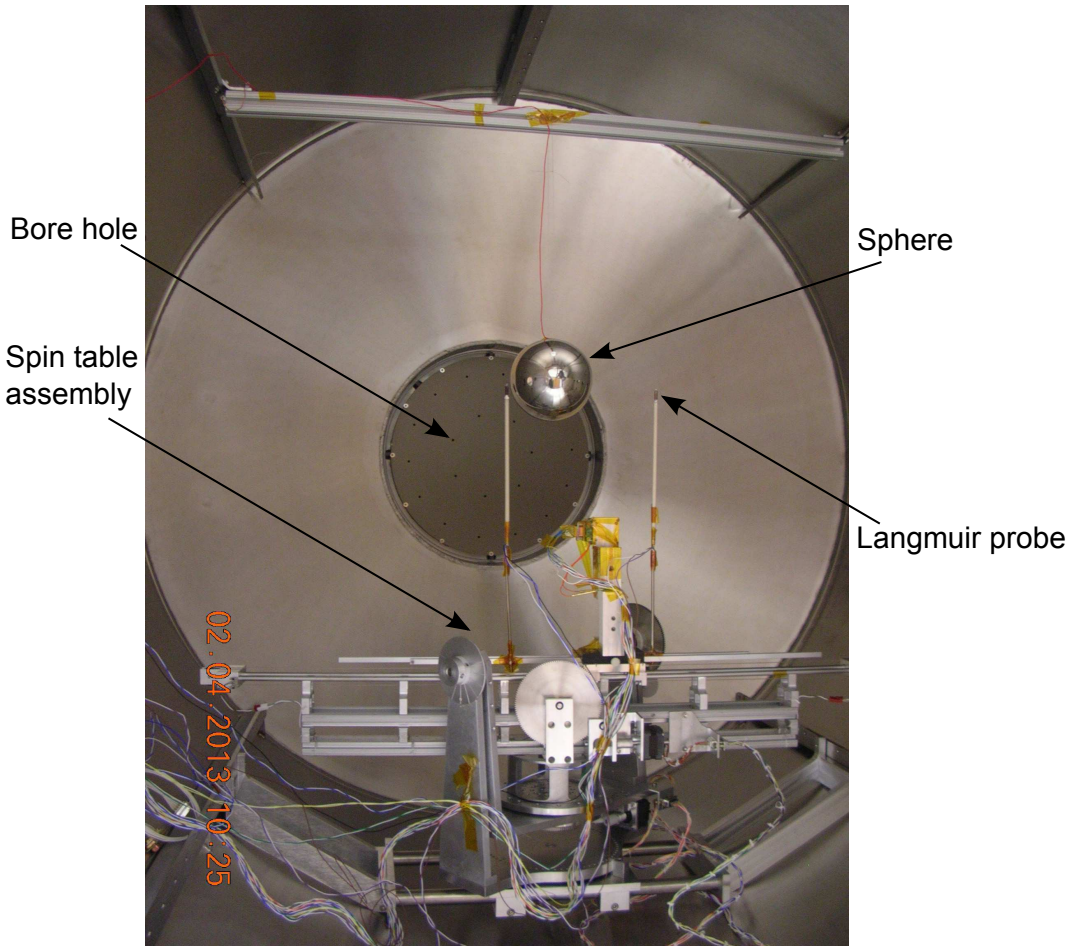

Figure 5.1: Inside view of the cylindrical vacuum chamber. The metal sphere is suspended by means of a thread and a horizontal beam. The two Langmuir probes are supported by thin and long cylindrical rods mounted to the spin table. This photo was provided by Lisa E. Gayetsky, Dartmouth College, USA.

The goal of the experiment was to study plasma properties in the vicinity of an immersed conducting body and thus develop a better understanding of the physics relevant to satellite-plasma interaction under well controlled laboratory conditions. More details about the experimental setup and plasma injection are found in [86, 87]. In this experiment, the plasma density and temperature were inferred by interpreting probe measurements using the orbital motion limited (OML) theory [8]. In order to assess the validity of the OML theory in this experiment, several simulations were made of the experiment, in which characteristics have been calculated at selected probe positions by account-

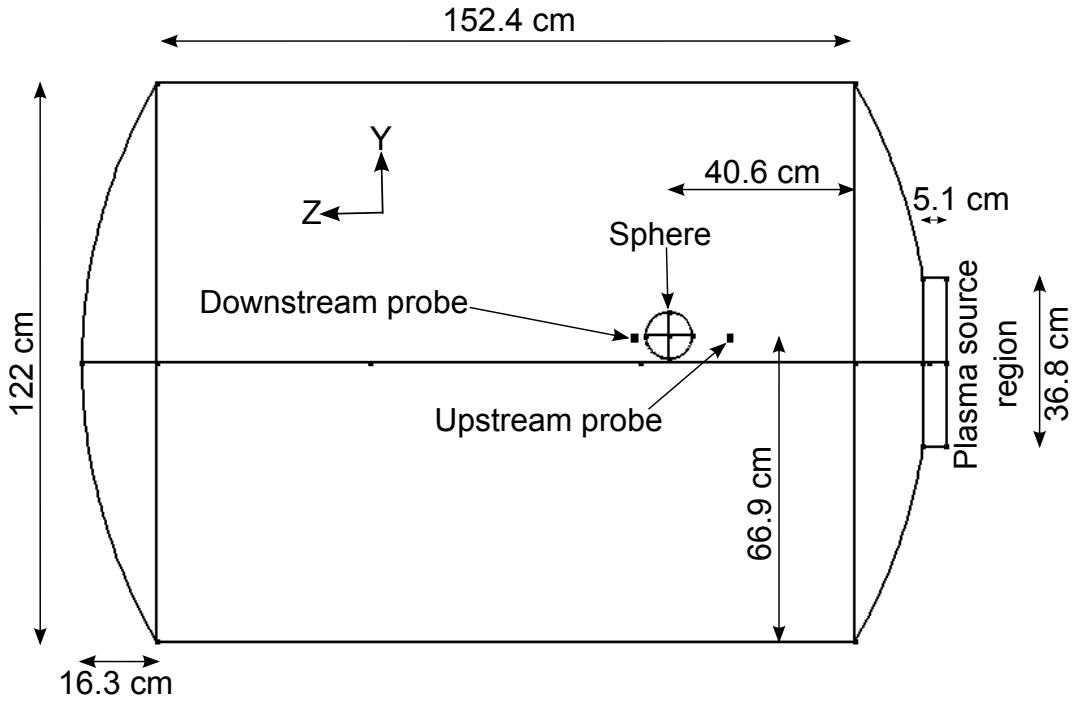

Figure 5.2: Geometry representing the experimental structures constructed with gmsh. The experiment consists of a vacuum vessel, a sphere, and two tiny cylindrical Langmuir probes. The probe closer to the source region is called the upstream probe whereas the one in the wake region is known as downstream probe. The spin table and some other structural details are not considered in the simulations, for simplicity. In this system of coordinate X is out of the page.

ing for actual probe geometry and compared with experimental measurements. This work was done in collaboration with Ms. Gayetsky. Simulations were made using PTetra, and the measured I-V characteristics are reproduced. In the following sections, the experiment modeling, I-V curves, and physics of the simulation results are described. The results presented in this chapter are being collated into a manuscript that will be submitted for publication.

5.2 Experiment modeling

The geometry of the experimental setup is constructed with gmsh, and it is illustrated in Fig. 5.2. We recall that this experiment was intended to simu-

late conditions similar to those that exist in the vicinity of a satellite in space. The satellite is represented by a conducting sphere located 5.874 cm above the midplane of the chamber. The vacuum chamber also contains two Langmuir probes supported by a spin table and various connection cables as shown in Fig. 5.1. The simulations account for accurate dimensions and main components therein, as well as for their relative positions. These components include the sphere and the two Langmuir probe tips. The isolating probe supports, the spin table, and the connecting wires are not included in the geometry for simplicity. The dimensions of the components provided by Ms. Gayetsky, and accounted for in the simulation are given in Table 5.1. The parameters of the injected

Table 5.1: Dimensions of the structures accounted for in the simulations.

Langmuir probe radius	0.16 cm
Langmuir probe length	1 cm
Sphere radius	5.08 cm
Plasma injection disc radius	18.4 cm
Chamber radius	61 cm
Chamber radius of curvature	106 cm
Chamber length	152 cm

plasma, including the local magnetic field and neutral density, are given in Table 5.2. In this table, variables identified with "TDB" are those that had to be determined experimentally from probe measurements. In the experiment, the unknown parameters are derived by applying OML theory. In the numerical modeling of the experiment, a trial and error approach was used to find the right combination of these parameters for which the experimental I-V curves are reproduced at two locations in the vacuum chamber, upstream and downstream of the sphere. Specifically, the electron density and temperature in the injection region are varied in order to best fit measured characteristics at both probe locations. That is, if an I-V characteristic is fitted at one point in the chamber by adjusting these parameters and, using the same parameters, the

Table 5.2: Measured and unknown plasma parameters to be determined (TBD).

Plasma drift velocity	$\vec{v_d} \simeq 7500\hat{z}$ m/s
Ion temperature	$T_i \simeq 0.3$ eV
Neutral density	$n_n \simeq 8 \times 10^{17}\mathrm{m}^{-3}$
Plasma density	$n_p \simeq 1 \times 10^{11}\mathrm{m}^{-3}$
Local magnetic field	$\vec{B} = (-11.45, -31.82, -6.02)\mu$T
Electron density	n_e =TBD
Electron temperature	T_e =TBD
Plasma potential	V_p =TBD

characteristic curves at other locations in the chamber are reproduced, then it is demonstrated that the model consistently simulate the experiment. It is noteworthy to mention that in the computer model an argon plasma is injected from the whole disc surface as well as the contiguous lateral surface rather than from the 21 bore holes in the injection disc as in the experiment. The actual plasma injection through the 21 bore holes would be very difficult to simulate for the following reasons. 1) A much higher plasma density would have to be modeled in each of the bore holes, characterized by significantly larger plasma frequency and smaller Debye length than in the vacuum chamber. 2) As a result, a very fine mesh, sufficient to resolve each hole as well as the Debye length, would be needed in the injection region. 3) Finally, due to the fact that the PTetra is explicit, and that most particles should not cross more than one cell in one timestep, very small timesteps would be required. Considering the fact that the sphere is at a distance of ~ 50 cm from the plasma source region, all of the 21 plasma beams are assumed to be well diffused before interacting with the sphere, and the sphere thus interacts with the central plasma beam which is assumed to be well described by a drifting Maxwellian plasma in the injection region. The problem then reduces to fitting the two measured characteristics with the computed ones by adjusting the density n and temperature T of the assumed drifting Maxwellian in the injection region. The numerical modeling

of the experiment is accomplished with PTetra, described in chapter 2. Both the Ar^+ ions and electrons are described fully kinetically with physical charges and masses. The simulations also account for the measured local magnetic field given in Table 5.2. Neutral particles are neglected in the simulations due to larger collisional mean free path > 1 m.

5.3 I-V characteristics

To compute the I-V characteristics, both upstream and downstream probes are biased simultaneously at discrete voltages with respect to the ground (the vacuum vessel). This is different from the experiment, in which characteristics are measured for only one probe at a time. That is, when a probe is biased to different voltages, the other one is left floating. By biasing both probes to the same potential in the simulations, it is possible to obtain the characteristics for both probes with half the simulation time of what would be required if each probe were biased individually. This procedure, however, is valid only if one probe's bias voltage has negligible influence on the other probe's characteristic, that is, if there is no 'crosstalk' between the probes. In order to assess crosstalk between the probes at locations shown in Fig. 5.2, two cases were simulated. In the first case, the upstream probe was biased to the highest voltage of +10 V, while the downstream probe was left floating. In the second case, the downstream probe was biased to +10 V, while the upstream probe was left floating. Compared to the simulations made with simultaneous biasing, case 1 showed no significant difference, and case 2 led to an increase in the collected current by the downstream probe by approximately 5%. It is therefore concluded that crosstalk is negligible, and that the simplification consisting of biasing both probes simultaneously to the same voltage leads to characteristics that are within 5% or less of the actual biasing procedure in which only one probe is biased at a time.

Using this approach, the best fit to the two characteristics measured with both probes led to $n_e = 1.5 \times 10^{11}\mathrm{m}^{-3}$ and $T_e = 0.58$ eV in the plasma injection region. A comparison between measured and computed characteristics is given in Fig. 5.3. For comparison the figure also shows characteristics obtained with a different (non optimal) density and temperature ($n_e = 1 \times 10^{11}\mathrm{m}^{-3}$ and $T_e = 0.3$ eV). It is important to mention that in PTetra these adjustable parameters are specified at plasma injection region only, and that the plasma density and temperature is determined self-consistently in the remainder of the vacuum chamber, from the PIC simulations. Figure 5.3 shows that an increase

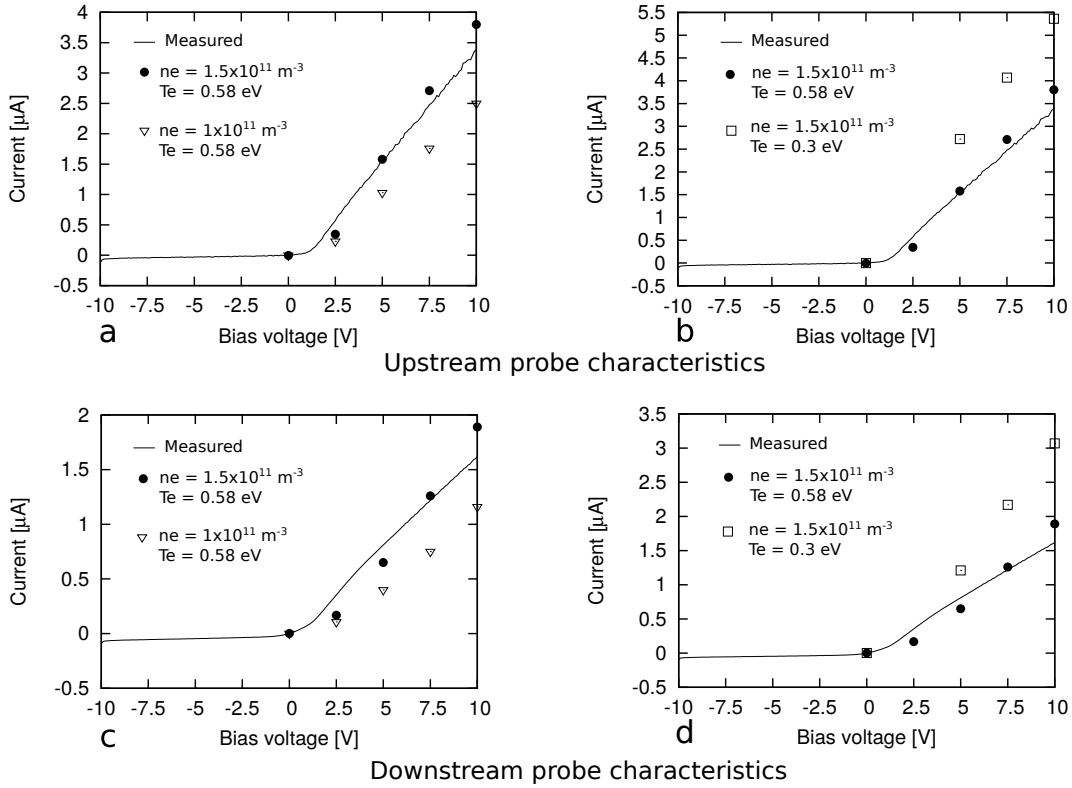

Figure 5.3: Comparison between the measured and computed I-V characteristics at the locations in the chamber shown in Fig. 5.2. Electron density and temperature effect on the curves computed by the upstream probe are shown in panels a and b respectively. Panels c and d show the effect of these parameters on the curves computed by the downstream probe.

in electron density causes more electron current collection by the probes, and

consequently, it leads to an increase in the slope of the curve, corresponding to the electron current collection. In contrast to electron density, a higher electron temperature results in a lower electron current collection by the probes. The comparison between the measured and computed curves in Fig. 5.3 shows that $T_e = 0.58$ eV and $n_e = 1.5 \times 10^{11}\text{m}^{-3}$ produce a good fit of the characteristics measured by both probes. Using the above fitted parameters at the injection side, a case is simulated without the probes to determine the unknown plasma parameters at the probe locations. The profiles of these parameters in the plane passing through the centre of sphere are shown in Fig. 5.4. It is noted that all three parameters considered (n_e, T_e, and ϕ) show significant spatial variations in the region of interest. This to be contrasted with uniform profiles assumed in the interpretation of probe measurements using the OML theory. A comparison of the measured electron density, temperature, and the plasma potential with the corresponding computed values, determined from Fig. 5.4, are presented in Table 5.3 for both upstream and downstream probes. The direct comparison

Table 5.3: Comparison between the measured and computed electron density (n_e), temperature (T_e), and plasma potential (V_p) relative to the vacuum chamber at upstream probe (Up) and downstream probe (Dp) positions.

Parameters	Measured		Computed	
	Up	Dp	Up	Dp
n_e (m^{-3})	3.17×10^{11}	9.58×10^{10}	1.22×10^{11}	1.61×10^{10}
T_e (eV)	0.45	0.54	0.57	0.39
V_p (V)	2.45	1.71	2.32	1.12

in Table 5.3 shows that OML theory provides a good estimate of the plasma temperature and potential but that the simulated and experimentally measured densities are significantly different. In particular, the temperature and plasma potential at the location of the upstream and downstream probes agree within 5% and 50%. Differences between measured and simulated densities, on the other hand, are of order 2.6 for the upstream probe and ~ 6 for the downstream probe. The larger differences found for the downstream probe are consistent

with the fact that particles are farther from a Maxwellian in the wake region. The large discrepancies between the densities is likely due to the breakdown of the OML theory under these experimental conditions due to presence of strong gradients in the plasma profiles and the fact, in particular, that the upstream distribution function is non Maxwellian.

5.4 Magnetic field effect on particle distributions

In order to assess the effect of the local magnetic field on the particle velocity distributions, a geometry without probes is simulated. Electron velocity distributions are computed by using the test-kinetic approach described in Chapter 2. It is found that due to their large mass and gyro-radius, argon ions are not affected by the local magnetic field, and their distributions are not shown here. Electron distribution functions are significantly affected by the magnetic field as shown in Fig. 5.5. These distributions are computed at a point close to the injection side, indicated by an arrow in Fig. 5.6. In the absence of a magnetic field, the electron distribution is a Maxwellian in the $V_x - V_y$ plane and a truncated Maxwellian in $V_z - V_x$ plane. The truncated Maxwellian is due to the fact that the electrons are drifting in the positive z direction and do not return back to the source region. This is why the distribution function vanishes there for $V_z < 0$. As shown in panel b and d of Fig. 5.5, the local magnetic field leads to complex structures in the electron distribution function. This complexity arises due to the Lorentz force experienced by the electrons. These filamentary structures are due to the electron thermal gyro-radius ~ 5 cm, being comparable to the linear dimension of the injection region, and the fact that the point being considered is not sufficiently far from the end of the injection chamber (for 5 cm from the end) for injected electrons to have isotropised. The structures in these distributions are further verified by plotting sample electron

trajectories. Figure 5.6 shows the trajectories of 100 electrons which are integrated backward in time from the point where these distribution functions are computed with $\vec{B}$ (red) and without $\vec{B}$ (green). This shows that the gyration along the field lines causes some electrons to turn around and propagate in the $-z$ direction at the point considered, thus leading to a non zero distribution function when $V_z < 0$ in panel d, and beak-like structure in the distribution in panel b.

5.5 Other features

In the simulation in which all of the structures, i.e., the chamber, sphere, and probes are grounded, the upstream probe collects positive current while the wake side probe collects negative current, as shown in panel a in Fig 5.7. The explanation is that the wake is mostly dominated by the fast moving electrons, and there are almost no ions to be collected. In this case, as both the sphere and upstream probe are negatively charged with respect to the surrounding plasma, the ion density plume between them is observed. A region of ion density enhancement behind the sphere also appears as the supersonic ion beams converges. In panel b in Fig 5.7, both probes are biased to the highest voltage relative to the grounded chamber walls. The wake formed behind the upstream probe overlaps the sheath surrounding the sphere. This phenomenon along with the ion repulsion from the positively biased probe effectively decrease the flow of ions to the sphere, and as a result the sphere becomes 8% more negative than it was when the upstream probe was grounded. Electron temperature effects on density profiles, in the chamber, are displayed in Fig. 5.8 for the case of grounded probes, and when the probes are biased to 10 V. A higher electron temperature causes faster radial expansion of the electrons (plasma). Consequently, the electron density disperses at the probes locations, and the probes collect less electron current as shown in panels b and d in Fig.

5.3. With grounded probes (top panel in Fig. 5.8), the sheath around the sphere looks like a pear; the wake behind the sphere becomes longer with decreasing T_e. The pear-like sheath turns into an apple-like structure when the probes have a higher positive bias voltage, and the wake is significantly modified. The electron density in the wake then increases, due to a positively biased probe in that region. Similarly, it follows that a higher electron temperature (T_e) results in faster radial expansion of argon ions as ions are being pulled in and out more strongly radially by the expanding electrons. The result is then a shorter wake behind the sphere.

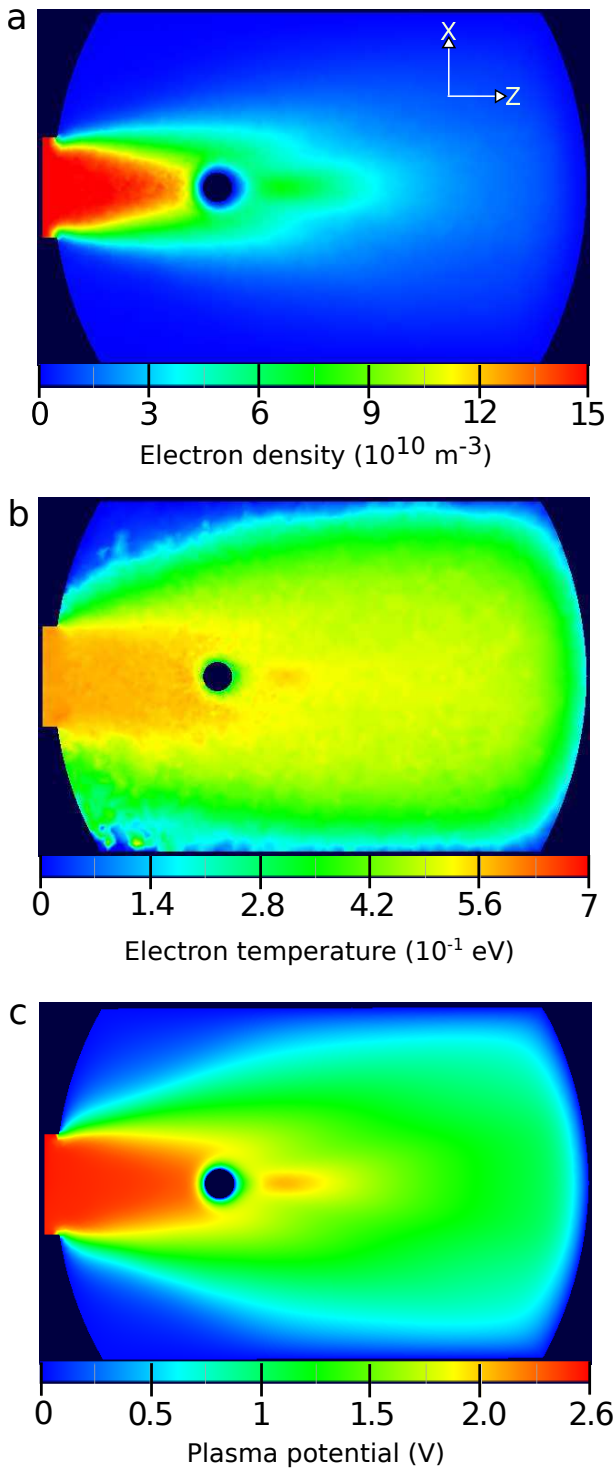

Figure 5.4: Electron density (panel a), temperature (panel b), and plasma potential (panel c) profiles in the plane passing through the centre of the sphere.

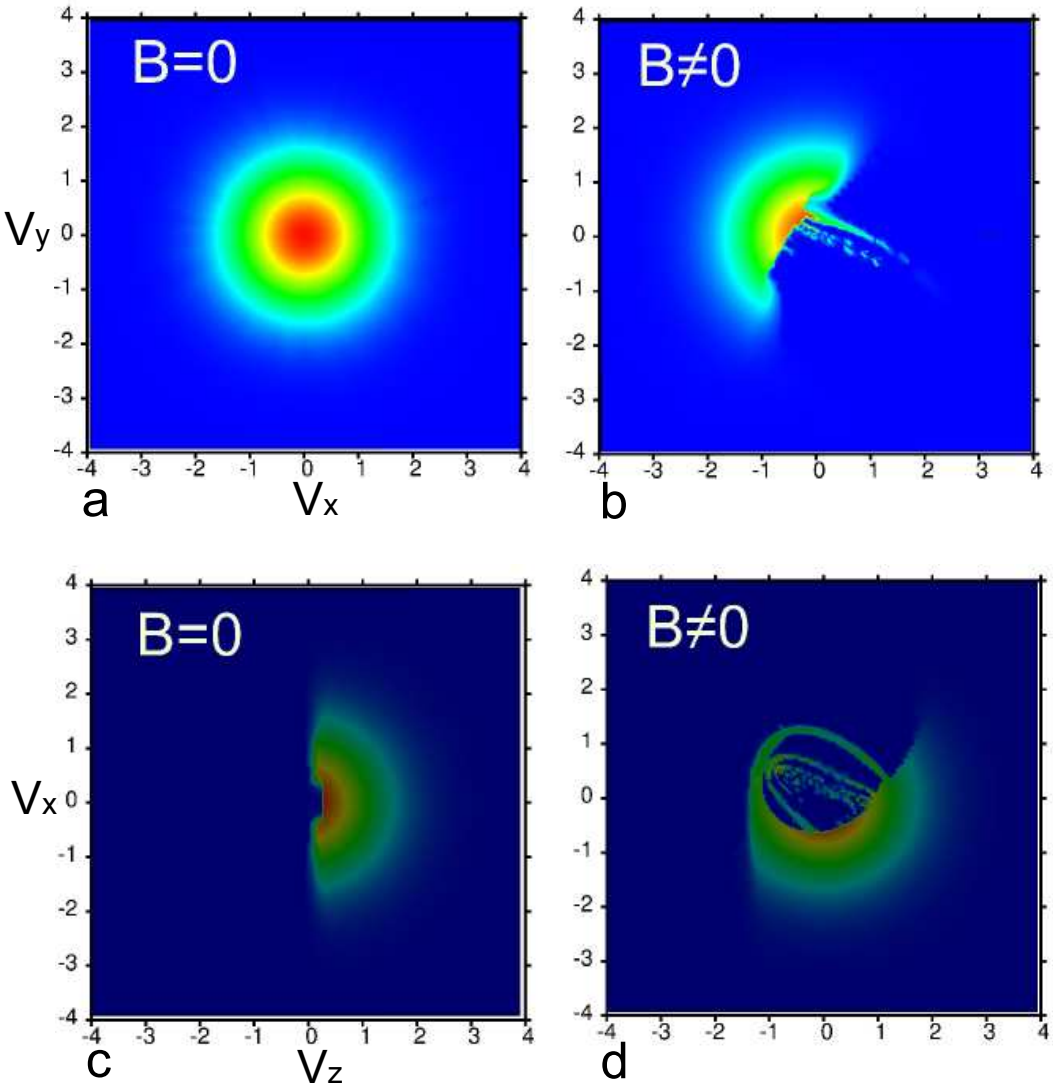

Figure 5.5: Electron velocity distribution functions at a distance of 5 cm from the source region with (panels b and d) and without magnetic field (panels a and c) are shown in a $V_x - V_y$ plane (top panels) and a $V_z - V_x$ plane (bottom panels). The velocities along the axes are normalized by the electron thermal velocity, $v_{th} = \sqrt{T_e/m_e}$.

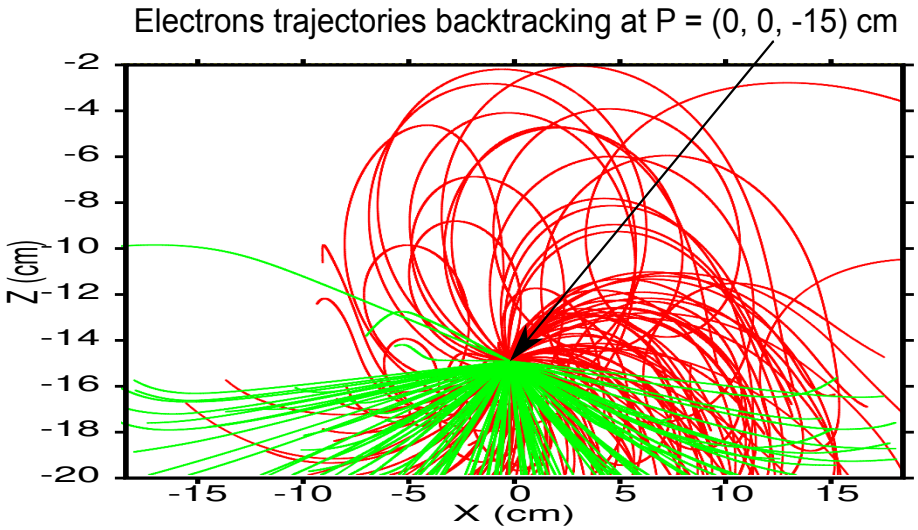

Figure 5.6: Electron trajectories computed with (red) and without (green) the local magnetic field. The trajectories are calculated using backtracking from the point shown in the figure. Numbers along the axes are in chamber coordinates; the entire x axis length corresponds to the diameter of the plasma injection disc.

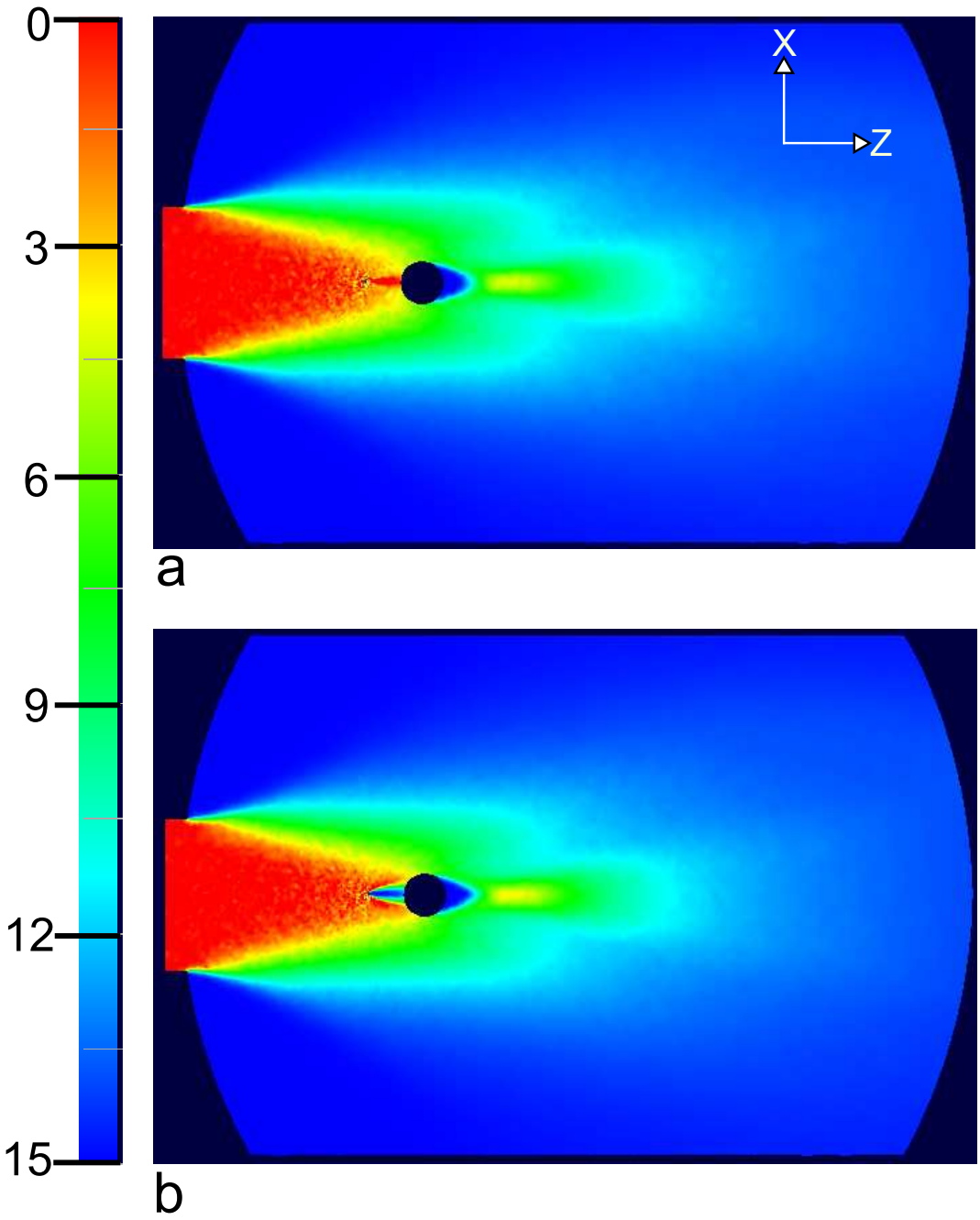

Figure 5.7: argon ion density ($\times 10^{10}\mathrm{m}^{-3}$) profiles in the $X - Z$ plane passing through the centre of the sphere. In panel a, the walls of the vacuum vessel, the sphere, and both probes are grounded. The profile in panel b corresponds to the case when both the probes are biased to 10 V with respect to the vessel and sphere.

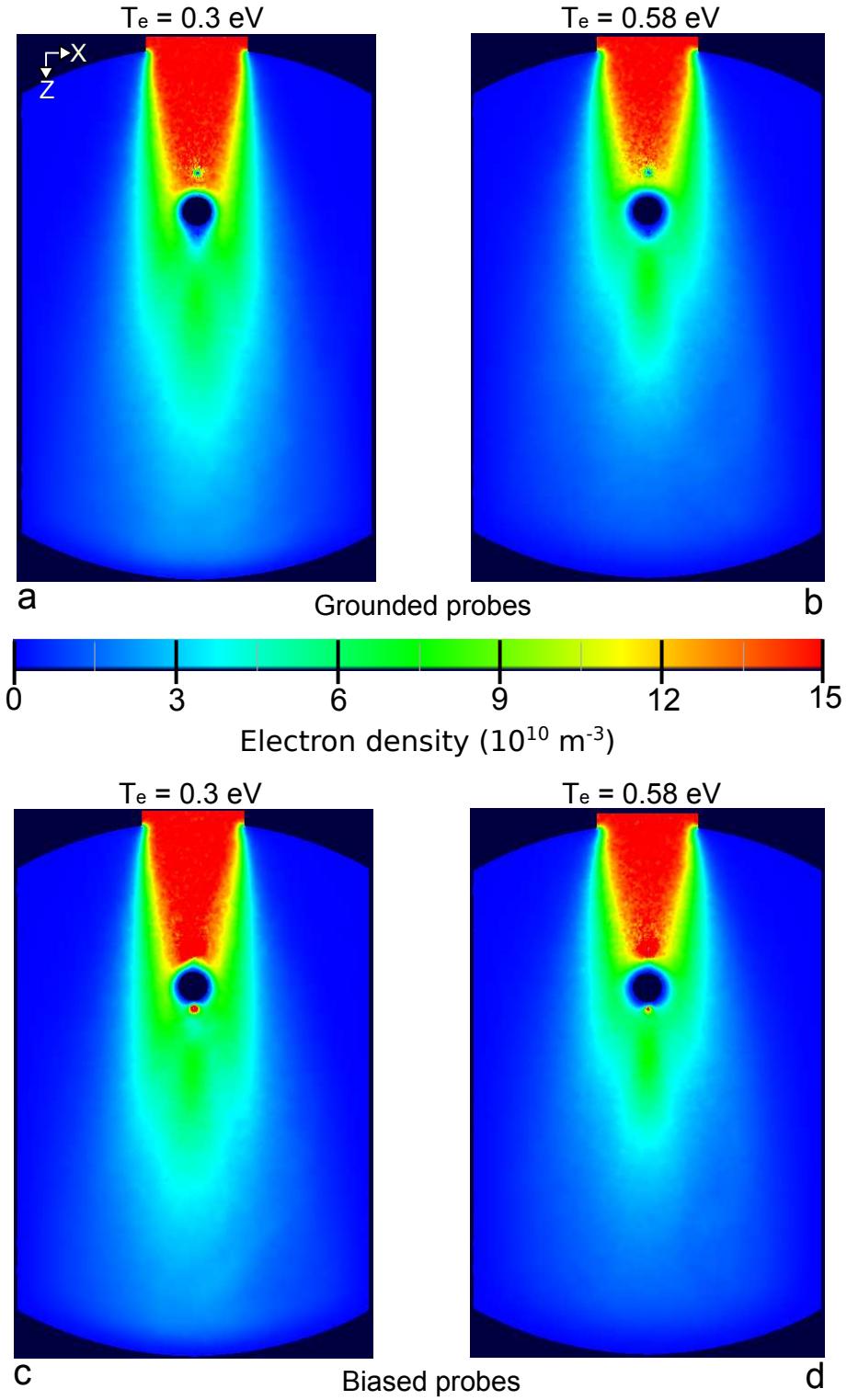

Figure 5.8: Electron density ($\times 10^{10}\mathrm{m}^{-3}$) profiles obtained with different electron temperatures (T_e) in the $X-Z$ plane passing through the centre of the sphere. The top panels correspond to simulation results in which both probes are grounded. The bottom panels show electron density profiles computed when both probes are biased to 10 V with respect to the vessel and sphere.

Chapter 6

Summary and conclusion

The objective of this dissertation is to study spacecraft interaction with space plasma and the effect of this interaction on the on-board sensor measurements. This thesis presents four related projects. In the first three, the interaction of space plasma with the recently launched Swarm satellites and the effects on its sensors, namely the electric field instrument (EFI) and magnetometers measurements, are investigated. The Swarm EFI consists of two thermal ion imagers (TIIs) and two spherical Langmuir probes. In the fourth project, a laboratory experiment is simulated, which was designed to study the physics of plasma-satellite interaction. These studies are made with a combination of PTetra and test-particle simulations. PTetra is a PIC code used to simulate the space plasma interaction with a satellite and its instruments.

In the first project, the interaction of space plasma with a simplified Swarm satellite and its TIIs is studied. The plasma parameters considered in the simulations correspond to those expected to be representative along Swarm orbits. The original contribution of this study is the consideration of Earth's magnetic field in the interaction between space plasma and plasma sensors, and the resulting perturbations in the measurements made with these instruments. PTetra is used to determine the spacecraft floating potential and the structure

of the electrostatic sheath surrounding the spacecraft. Using the potential field obtained with PTetra, particle backtracking and Liouville's theorem applied to the one-particle distribution function were used to compute H^+ and O^+ ion distribution functions around the aperture of each TII and at the tips of the probes. These distribution functions were then used as input in Monte Carlo simulations of ions entering the sensors, down to the micro channel plate (MCP), where detailed fluxes were computed on a 32×64 pixel array. Three cases were considered, including a reference case without magnetic field, and two with magnetic fields $\vec{B} = \mp 4 \times 10^{-5}\mathrm{T}\hat{z}$ expected near the North and South geographic poles respectively. The local magnetic field and the associated $-\vec{v} \times \vec{B}$ electric field, where $\vec{v}$ is the plasma flow velocity in the spacecraft reference frame, are found to lead to asymmetries in the distribution function of ions at the aperture of TIIs. This in turn leads to shifts in the centroid of ion flux profiles on the MCP, with hydrogen being significantly more affected than the heavier oxygen ions. The estimates indicate that the shifts in the O^+ flux centroids associated with magnetic field effects could lead to aberrations in the inferred lateral velocity by as much as $\simeq \pm 200$ m/s. These aberrations would be systematic and periodic, as the magnitude and orientation of the magnetic field would vary along the Swarm orbits. Therefore it is concluded that an optimal interpretation of TII measurements will require that shifts induced by magnetic fields and associated $-\vec{v} \times \vec{B}$ electric fields be modeled and accounted for in the calibration of the instruments. In addition to Swarm, these terrestrial magnetic field effects will be important for low Earth orbit spacecraft measurements of ion velocity and electric field in general. Future study should include simulations with more detailed geometry of Swarm satellite, various biasing scenarios of the face plate and the different parts of TII shells consistent with actual operational conditions of the orbiting Swarm satellites.

The Langmuir probes that are part of the EFI on Swarm are studied in the second project. The inferred electric field from the potential difference of both probes is in good agreement (relative difference $\sim 10\%$) with the expected value. Possible crosstalk between the probes was assessed by comparing collected currents computed when the two probes have the same bias (± 5 V for both) and opposite bias (± 5 V on one and ∓ 5 V on the other) voltages. The currents were essentially the same in both cases, which indicates that for the parameters considered, crosstalk should be negligible. This conclusion is expected to hold for other plasma parameters and magnetic fields encountered along the Swarm orbits. Crosstalk, however, would likely be important if the two probes were within a common magnetic flux tube of radius of order two thermal electron gyro-radius (~ 6 cm). This should not occur under normal operations, with Swarms' nearly polar orbits. It could occur however, in testing or calibration maneuvers, if Swarm's yaw angle were varied by $\sim \pm 90°$. Characteristics were calculated for the two Langmuir probes while accounting for a detailed description of the probes' geometry and a simplified description of the payload. The presence of a background $-\vec{v} \times \vec{B}$ electric field is found to cause significant distortions in the equipotentials near the Langmuir probes. These in turn will affect particle velocity distributions and they will impact measurements made with these sensors. No significant difference is found between the left and right probe characteristics, whether magnetic field effects are taken into account or not. Collected electron currents computed with positive bias, on the other hand, are found to be appreciably larger when no magnetic field is taken into account. This is a consequence of electron's weak magnetization and the fact that collected electrons are effectively constrained to be contained in a magnetic flux tube of radius of order two electron gyro-radii.

The third project presents the first fully kinetic simulation results leading to quantitative estimates of magnetic field perturbations associated with the

interaction between a satellite and space environment. The analysis is based on a first order estimate of the perturbed fields using PTetra in which the effect of magnetic field perturbations on particle trajectories is not taken into account. The validity of this approach is verified a posteriori, as the computed perturbed magnetic fields are smaller than the background field, by six orders of magnitude or more. The results reveal some interesting features of spacecraft-plasma induced perturbed current density and magnetic field. In particular, due to the absence of shielding of current density perturbations at steady state, and due to electron magnetization, these currents and associated perturbed magnetic fields extend along the magnetic field over distances comparable to or larger than the linear scale of the satellite itself. In the case considered, for Swarm near the North magnetic pole, computed perturbations at the magnetometer locations are well below the instruments' sensitivity threshold. Direct magnetic field measurements made by Swarm will therefore be purely geophysical in origin and no corrections will be needed to account for possible aberrations caused by spacecraft-environment interaction. As the satellites fly over the North pole, however, it is predicted that under certain conditions, there will be small but systematic variations in the perturbed magnetic field. These variations will occur when the satellites cross the terminator during certain orbit epochs. They will be caused by photo-electrons being turned on and off over a period of approximately 30s. While the perturbations, of order $|\delta\vec{B}| \sim 2\text{pT}$, are too small to be measured directly, they might be detectable by taking averages over several similar crossings. Looking at possible future similar missions to Venus or Mercury, magnetic field perturbations should likely be significantly more important, owing to the larger solar UV flux and photo-emission in these environments. In such missions, the satellite geometry and the configuration of the magnetometers would likely have to account for satellite-environment induced magnetic perturbations, and corrections in the interpretation of the measurements might be required in order to account for spacecraft-induced

magnetic field perturbations.

In the fourth and final project, kinetic modeling of a laboratory experiment is accomplished fully kinetically with PTetra. In the experiment, a supersonic argon plasma jet interacting with a grounded conducting spherical body, contained in a vacuum chamber, is studied using two cylindrical Langmuir probes. The experiment conducted under well controlled and diagnosed conditions, was designed to study some basic physics of relevance to satellite interaction with the space environment. The current-voltage (I-V) characteristics of the probes were measured in the vicinity of the sphere, one located upstream and the other one downstream, in the wake region. In the experiment, the electron density, temperature, and the plasma potential are derived from the measured curves by using standard analysis technique. In the simulations, the plasma parameters (density and temperature) in the injection region are determined by trial and error so as to best fit measured characteristics at the two probe locations. The electron density and temperature obtained from the simulations at the probe locations are then compared with experimentally measured values. The comparison showed that the standard analysis technique although not strictly valid for the experimental situation, still gives an estimate of the parameters which proves helpful in initiating the computer simulations. In particular, contrary to the assumptions made in the standard technique 1) the electrons are magnetized in the presence of geomagnetic field, 2) there is a radial plasma density gradient in the chamber, and 3) the electron distribution function is non-Maxwellian. This study showed PTetra capability and power for modeling a laboratory experiment.

In summary, the most significant contributions of my research work in this thesis are as follows:

- Provide the first quantitative estimate of aberrations in the measurements of the plasma flow velocity made with EFI, while accounting for Earth magnetic field.

- Provide the first estimate of magnetic field effects on Swarm Langmuir probe characteristics, and assessment of possible crosstalk between the two nearby probes. This was done while accounting for a good fraction of the ram section of the spacecraft body.

- Provide the first fully kinetic estimate of magnetic field perturbations associated with the interaction between a spacecraft (Swarm) and surrounding plasma. This was done while accounting for the full length ($\sim$ 9.2 m) of the satellite, and a detailed representation of the boom geometry.

- Apply PTetra to reproduce measurements made in a laboratory experiment designed to study satellite-plasma interaction under well controlled conditions.

Finally, if the following addition of physics modules or improvements in the numerical algorithms could be made to PTetra, the resulting model would have a significantly broader range of applicability:

- Include charge exchange effects.

This would allow simulations of a charge exchange in thruster plasma as well as in a variety of laboratory and space plasmas where charge exchange is important.

- Generalization of the code to handle distribution functions other than the (drifting or non-drifting) Maxwellian distribution.

This would enable PTetra to simulate the interaction of super-thermal (or any other distribution functions) electrons and ions with the spacecraft.

- Upgrade the model to describe electric and magnetic perturbations self consistently.

This improvement would broaden the range of applicability of PTetra to electromagnetic perturbations or to electromagnetic waves propagating in plasmas. This would include, for example, the interaction of electric field measuring antennas with space plasma and the study of electromagnetic waves, e.g., Alfvén waves.

Bibliography

[1] E. C. Whipple, "Potentials of surfaces in space," *Rep. Prog. Phys.*, vol. 44, pp. 1197–1250, 1981.

[2] J. Robinson, P.A. and P. Coakley, "Spacecraft charging-progress in the study of dielectrics and plasmas," *IEEE Trans. Electr. Insul.*, vol. 27, no. 5, pp. 944 – 60, 1992.

[3] A. R. Martin, "A review of spacecraft/plasma interactions and effects on space systems," *J. British Interplanetary Society*, vol. 47, pp. 134–142, 1994.

[4] A. Tribble, *The Space Environment: Implications for Spacecraft Design.* Princeton USA: Princeton University Press, 2003.

[5] D. Hastings and H. Garrett, *Spacecraft-Environment Interactions.* Cambridge UK: Cambridge University Press, 2004.

[6] S. Lai, *Fundamentals of spacecraft charging.* Princeton USA: Princeton University Press, 2012.

[7] I. Langmuir and H. Mott-Smith, Jr., "Studies of electric discharges in gases at low pressures," *General Electric Review*, vol. 27, no. 12, pp. 810 – 820, 1924.

[8] H. Mott-Smith and I. Langmuir, "Theory of collectors in gaseous discharges," *Physical Review*, vol. 28, pp. 727 – 763, 1926.

[9] B. Jung, "Die Entstehung fester Partikel im interstellaren Raum," *Astronomische Nachrichten*, vol. 263, p. 425, 1937.

[10] Spitzer, L., Jr., "Dynamics of the interstellar medium. I. Local equilibrium," *Astrophysical Journal*, vol. 93, pp. 369 – 379, 1941.

[11] ——, "The temperature of interstellar matter. I," *Astrophysical Journal*, vol. 107, pp. 6 – 33, 1948.

[12] B. Lehnert, "Electrodynamic effects connected with the motion of a satellite of the earth," *Tellus*, vol. 8, pp. 408–409, 1956.

[13] K. I. Gringauz and M. K. Zelikman, "Measuring the concentration of positive ions along the orbit of an artificial earth satellite (in Russian)," *Uspekhi Fiz. Nauk*, vol. 63, pp. 239–252, 1957.

[14] I. M. Imyanitou, "Electrostatic filed measurements in the Earth's upper atmosphere (in Russian)," *Uspekhi Fiz. Nauk*, vol. 63, pp. 267–282, 1957.

[15] D. B. Beard and F. S. Johnson, "Charge and magnetic field interaction with satellites," *J. Geophys. Res.*, vol. 65, pp. 1–7, 1960.

[16] J. E. C. Whipple, "The equilibrium electric potential of a body in the upper atmosphere and in interplanetary space," *PhD dissertation*, 1965.

[17] G. L. Gdalevich, "Measurement of electrostatic field strength at the surface of a rocket flying in the ionosphere (in Russian)," *Doklady AN SSSR, Geof.*, vol. 146, p. 1064, 1962.

[18] I. M. Imyanitov, G. L. Gdalevich, and Y. M. Shvarts, "Measurement of electrostatic field strength at the surface of geophysical rockets flying in the Earth's upper atmosphere (in Russian)," *Iskusstv. Sputniki Zemli*, vol. 17, p. 66, 1963.

[19] R. Sagalyn, M. Smiddy, and J. Wisnia, "Measurement and interpretation of ion density distributions in the daytime F region," *J. Geophys. Res.*, vol. 68, no. 1, pp. 199 – 211, 1963.

[20] S. E. DeForest, "Spacecraft charging at synchronous orbit," *J. Geophys. Res.*, vol. 77, pp. 651–659, 1972.

[21] I. Katz, D. Parks, M. Mandell, J. Harvey, S. Wang, and J. Roche, "NASCAP, a three-dimensional charging analyzer program for complex spacecraft," *IEEE Trans. Nucl. Sci.*, vol. 24, no. 6, pp. 2276 – 80, 1977.

[22] N. Stevens and J. C. Roche, "Nascap modelling of environmental-charging-induced discharges in satellites." *IEEE Trans. Nucl. Sci.*, vol. 26, no. 6, pp. 5112 – 5120, 1979.

[23] N. Stevens, "Modelling of environmentally induced discharges in geosynchronous satellites," *IEEE Trans. Nucl. Sci.*, vol. 27, no. 6, pp. 1792 – 6, 1980.

[24] C. Enloe, D. Cooke, W. Pakula, M. Violet, D. Hardy, C. Chaplin, R. Kirkwood, M. Tautz, N. Bonito, C. Roth, G. Courtney, V. Davis, M. Mandell, D. Hastings, G. Shaw, G. Giffin, and R. Sega, "High-voltage interactions in plasma wakes: results from the charging hazards and wake studies (chaws) flight experiments," *J. Geophys. Res.*, vol. 102, no. A1, pp. 425 – 33, 1997.

[25] V. Davis, M. Mandell, D. Cooke, and C. Enloe, "High-voltage interactions in plasma wakes: simulation and flight measurements from the charge hazards and wake studies (chaws) experiment," *J. Geophys. Res.*, vol. 104, no. A6, pp. 12 445 – 59, 1999.

[26] M. Mandell, V. Davis, D. Cooke, A. Wheelock, and C. Roth, "NASCAP-2k spacecraft charging code overview," *IEEE Trans. Plasma Sci.*, vol. 34, no. 5, pp. 2084 – 93, 2006.

[27] M. Mandell, D. Cooke, V. Davis, G. Jongeward, B. Gardner, R. Hilmer, K. Ray, S. Lai, and L. Krause, "Modeling the charging of geosynchronous and interplanetary spacecraft using NASCAP-2k," *Adv. Space Res.*, vol. 36, no. 12, pp. 2511 – 15, 2005.

[28] M. M. Donegan, J. L. Sample, J. Dennison, and R. Hoffmann, "Spacecraft coating-induced charging: A materials and modeling study of environmental extremes," *Journal of Spacecraft and Rockets*, vol. 47, no. 1, pp. 134 – 146, 2010.

[29] J.-F. Roussel, F. Rogier, G. Dufour, J.-C. Mateo-Velez, J. Forest, A. Hilgers, D. Rodgers, L. Girard, and D. Payan, "SPIS open-source code: Methods, capabilities, achievements, and prospects," *IEEE Trans. Plasma Sci.*, vol. 36, no. 5 PART 2, pp. 2360 – 2368, 2008.

[30] T. Muranaka, S. Hosoda, J. Kim, S. Hatta, K. Ikeda, T. Mamanaga, M. Cho, H. Usui, H. O. Ueda, K. Koga, and T. Goka, "Development of multi-utility spacecraft charging analysis tool (MUSCAT)," *IEEE Trans. Plasma Sci.*, vol. 36, no. 5, pp. 2336 – 49, 2008.

[31] J. Yang, X.-X. Chen, J. Zhou, and S.-H. Xia, "Investigation of the influence of wake effect on plasma sheath," *Yuhang Xuebao/Journal of Astronautics*, vol. 31, no. 2, pp. 531 – 535, 2010.

[32] S. Guillemant, V. Genot, J.-C. Mateo-Velez, R. Ergun, and P. Louarn, "Solar wind plasma interaction with solar probe plus spacecraft," *Ann. Geophys.*, vol. 30, no. 7, pp. 1075 – 92, 2012.

[33] S. Guillemant, V. Genot, J.-C. Velez, P. Sarrailh, A. Hilgers, and P. Louarn, "Simulation study of spacecraft electrostatic sheath changes with the heliocentric distances from 0.044 to 1 AU," *IEEE Trans. Plasma Sci.*, vol. 41, no. 12, pp. 3338 – 48, 2013.

[34] V. Davis, M. Mandell, D. Cooke, A. Wheelock, J.-C. Mateo-Velez, J.-F. Roussel, D. Payan, M. Cho, and K. Koga, "Comparison of Low Earth Orbit Wake Current Collection Simulations Using Nascap-2k, SPIS, and MUSCAT Computer Codes," *IEEE Trans. Plasma Sci.*, vol. 41, no. 12, pp. 3303 – 9, 2013.

[35] R. Marchand, Y. Miyake, H. Usui, J. Deca, G. Lapenta, J. C. Mato-Vlez, R. E. Ergun, A. Sturner, V. Gnot, A. Hilgers, and S. Markidis, "Cross-comparison of spacecraft-environment interaction model predictions applied to solar probe plus near perihelion," *Phys. Plasmas*, vol. 21, pp. 062 901–1 062 901–12, 2014.

[36] E. Friis-Christensen, H. Luhr, and G. Hulot, "Swarm: a constellation to study the Earth's magnetic field," *Earth, Planets and Space*, vol. 58, no. 4, pp. 351 – 8, 2006.

[37] E. Friis-Christensen, H. Luhr, D. Knudsen, and R. Haagmans, "Swarm - an Earth Observation Mission investigating geospace," *Adv. Space Res.*, vol. 41, no. 1, pp. 210 – 16, 2008.

[38] F. Mobley, L. Eckard, G. Fountain, and G. Ousley, "MAGSAT–A new satellite to survey the Earth's magnetic field," *IEEE Trans. Magnetics*, vol. 16, p. 758, 1980.

[39] T. Moretto, E. Friis-Christensen, J. W. Gjerlov, N. Olsen, and F. Primdahl, "The Near-Earth Magnetic Satellite Missions, Ørsted and SAC-C/Ørsted-2, in Relation to the Cluster-II Mission," *Cluster-II Workshop Multiscale/Multipoint Plasma Measurements*, vol. 449, p. 363, 2000.

[40] C. Reigber, H. Lühr, L. Grunwaldt, C. Förste, R. König, H. Massmann, and C. Falck, *Observation of the Earth System from Space: CHAMP mission 5 years in orbit.* Berlin, Germany: Springer, 2006.

[41] N. Olsen, H. Luhr, T. Sabaka, M. Mandea, M. Rother, L. Toeffner-Clausen, and S. Choi, "CHAOS - a model of the Earth's magnetic field derived from CHAMP, Orsted, and SAC-C magnetic satellite data," *Geophys. J. Int.*, vol. 166, no. 1, pp. 67 – 75, 2006.

[42] C. Finlay, S. Maus, C. Beggan, T. Bondar, A. Chambodut, T. Chernova, A. Chulliat, V. Golovkov, B. Hamilton, M. Hamoudi, R. Holme, G. Hulot, W. Kuang, B. Langlais, V. Lesur, F. Lowes, H. Luhr, S. Macmillan, M. Mandea, S. McLean, C. Manoj, M. Menvielle, I. Michaelis, N. Olsen, J. Rauberg, M. Rother, T. Sabaka, A. Tangborn, L. Tffner-Clausen, E. Thebault, A. Thomson, I. Wardinski, Z. Wei, and T. Zvereva, "International geomagnetic reference field: The eleventh generation," *Geophys. J. Int.*, vol. 183, no. 3, pp. 1216 – 1230, 2010.

[43] G. Hulot, C. Eymin, B. Langlais, M. Mandea, and N. Olsen, "Small-scale structure dynamics of the geodynamo inferred from Oersted and Magsat satellite data," *Nature*, vol. 416, p. 620 623, 2002.

[44] N. Olsen and M. MANDEA, "Will the Magnetic North Pole Move to Siberia?" *Eos Trans. AGU*, vol. 88, pp. 293–300, 2007.

[45] L. Newitt, A. Chulliat, and J.-J. Orgeval, "Location of the North Magnetic Pole in April 2007," *Earth, Planets and Space*, vol. 61, no. 6, pp. 703 – 10, 2009.

[46] R. Coe, M. Prevot, and P. Camps, "New evidence for extraordinarily rapid change of the geomagnetic field during a reversal," *Nature*, vol. 374, no. 6524, pp. 687 – 687, 1995.

[47] G. Glatzmaier and P. Roberts, "A three-dimensional self-consistent computer simulation of a geomagnetic field reversal," *Nature*, vol. 377, no. 6546, pp. 203 – 9, 1995.

[48] C. Constable, "Link between geomagnetic reversal paths and secular variation of the field over the past 5 myr," *Nature*, vol. 358, no. 6383, pp. 230 – 230, 1992.

[49] R. Gubbins, D. & Coe, "Longitudinally confined geomagnetic reversal paths from non-dipole transition fields," *Nature*, vol. 362, pp. 51 – 53, 1993.

[50] H. Svensmark and E. Friis-Christensen, "Variation of cosmic ray flux and global cloud coverage A missing link in solar-climate relationships," *J. Atmos. Sol. Terr. Phys.*, vol. 59, p. 1225 1232, 1997.

[51] L. Vieira and L. da Silva, "Geomagnetic modulation of clouds effects in the Southern Hemisphere Magnetic Anomaly through lower atmosphere cosmic ray effects," *Geophys. Res. Lett.*, vol. 33, no. 14, p. 5 pp., 2006.

[52] [Online]. Available: http://www.esa.int/ESA/Our_Missions.

[53] S. Rehman, J. Burchill, A. Eriksson, and R. Marchand, "Earth magnetic field effects on Swarm electric field instrument," *Planet. Space Sci.*, vol. 73, pp. 145 –150, 2012.

[54] S. U. Rehman, R. Marchand, J.-J. Berthelier, T. Onishi, and J. Burchill, "Earth magnetic field effects on particle sensors on LEO satellites," *IEEE Trans. Plasma Sci.*, vol. 41, no. 12, pp. 3402 – 3409, 2013.

[55] S. ur Rehman and R. Marchand, "Plasma-satellite interaction driven magnetic field perturbations," *Phys. Plasmas*, vol. 21, p. 090701 (5 pp.), 2014.

[56] C. Geuzaine and J.-F. Remacle, "Gmsh: A 3-D finite element mesh generator with built-in pre- and post-processing facilities," *Int. J. Numer. Methods Eng.*, vol. 79, no. 11, p. 13091331, 2009.

[57] R. Marchand, "PTetra, a Tool to Simulate Low Orbit Satellite-Plasma Interaction," *IEEE Trans. Plasma Sci.*, vol. 40, no. 2, pp. 217 – 29, 2012.

[58] R. Hockney and J. Eastwood, *Computer simulation using particles*. USA: McGraw-Hill Inc, 1981.

[59] C. Birdsall and A. Langdon, *Plasma physics via computer simulation*. USA: McGraw-Hill Inc, 1985.

[60] O. C. Zienkiewicz and R. L. Taylor, *The Finite Element Method*. New York, USA: McGraw-Hill, 1989.

[61] Y. Saad, *Iterative Methods for Sparse Linear Systems*. Philadelphia, PA, USA: SIAM, 2003.

[62] T. Speiser, "Particle trajectories in a model current sheet, based on the open model of the maghetosphere, with applications to auroral particles," *J. Geophys. Res.*, vol. 70, pp. 1717–28, 1965.

[63] D. Delcourt, "Particle acceleration by inductive electric fields in the inner magnetosphere," *J. Atmos. Sol. Terr. Phys. 64, 551.*, vol. 64, pp. 551–9, 2002.

[64] S. Takeuchi, "New particle accelerations by magnetized plasma shock waves," *Phys. Plasmas*, vol. 12, pp. 102 901–6, 2005.

[65] M. Mendillo, J. Emery, and B. Flynn, "Modeling the moon's extended sodium as a tool for investigating sources of transient asmospheres," *Adv. Space Res.*, vol. 19, pp. 1577–86, 1997.

[66] T. E. Moore, M.-C. Fok, M. O. Chandler, R. C. Chappell, S. P. Christon, D. C. Delcour, J. Fedder, M. Huddleston, M. Liemohn, W. K. Peterson, and S. Slinker, "Plasma sheet and (nonstorm) ring current formation from solar and polar wind sources," *J. Geophys. Res, A, Space Phys.*, vol. 110, pp. A02 210, doi:10.1029/2004JA010 563, 2005.

[67] T. Moore, M.-C. Fok, D. Delcourt, S. Slinker, and J. Fedder, "Global aspects of solar wind-ionosphere interactions," *J. Atmos. Sol.-Terr. Phys.*, vol. 69, no. 3, pp. 265–78, 2007.

[68] D. Delcourt, F. Leblanc, K. Sekic, N. Teradad, T. Mooree, and M.-C. Fok, "Ion energization during substorms at mercury," *Planet. Space Sci.*, vol. 55, pp. 1502–1508, 2007.

[69] R. Richard, R. Walker, and M. Ashour-Abdalla, "The population of the magnetosphere by solar winds ions when the interplanetary magnetic field is northward," *Geophys. Res. Lett.*, vol. 21, pp. 2455–8, 1994.

[70] R. Marchand, J. L. F. Mackay, and K. Kabin, "Consistency check of a global MHD simulation using the test-kinetic approach," *Plasma Phys. Cont. Fusion*, vol. 50, pp. 074 007 1–10, 2008.

[71] R. Marchand, "Test-particle simulation of space plasmas," *Commun. Comput. Phys.*, vol. 8, no. 3, pp. 471–483, 2010.

[72] G. Voitcu and M. Echim, "Ring-shaped velocity distribution functions in energy-dispersed structures formed at the boundaries of a proton stream injected into a transverse magnetic field: Test-kinetic results," *Phys. Plasmas*, vol. 19, pp. 022 903–022 903, 2012.

[73] R. M. Gabriel Voitcu, Marius Echim, "Comparative study of forward and backward test-kinetic simulation approaches," *Comput. Phys. Commun.*, vol. 183, pp. 2561–2569, 2012.

[74] R. Marchand, J. Burchill, and D. Knudsen, "Modelling electrostatic sheath effects on Swarm electric field instrument measurements," *Space Sci. Rev.*, vol. 156, no. 1-4, pp. 73 – 87, 2010.

[75] M. Chiaretta, "Numerical Modelling of Langmuir Probe Measurements for the Swarm Spacecraft," *Diploma dissertation*, 2011.

[76] D. Knudsen, J. Burchill, K. Berg, T. Cameron, G. Enno, C. Marcellus, E. King, I. Wevers, and R. King, "A low-energy charged particle distribution imager with a compact sensor for space applications," *Rev. Sci. Instrum.*, vol. 74, no. 1, pp. 202 – 11, 2003.

[77] L. H. Fisher and R. N. Varney, "Contact potentials between metals: history, concepts, and persistent misconceptions," *Am. J. Phys.*, vol. 44, pp. 464–75, 1976.

[78] J. Allen, "Probe theory - the orbital motion approach," *Phys. Scr.*, vol. 45, pp. 497 – 503, 2012.

[79] L. Tonks and I. Langmuir, "Oscillations in ionized gases," *Phys. Rev.*, vol. 33, p. 195, 1929.

[80] M. J. Mandell, V. A. Davis, D. L. Cooke, A. T. Wheelock, and C. J, "NASCAP-2k spacecraft charging code overview," *IEEE Trans. Plasma Sci.*, vol. 34, pp. 2084–93, 2006.

[81] J. F. Roussel, F. Rogier, D. Volpert, G. Dufour, J. C. Mato-Vlez, J. Forest, and A. Hilgers, "Spacecraft plasma interaction software (SPIS): Numerical solvers methods and architecture," *JAXA Special Publication*, vol. JAXA-SP-05-001E, pp. 462–472, 2005.

[82] J. Roussel, F. Rogier, G. Dufour, J. Matéo-Vélez, J. Forest, A. Hilgers, D. Rogers, L. Girard, and D. Payan, "SPIS open-source code: Methods, capabilities, achievements and prospects," *IEEE Trans. Plasma Sci.*, vol. 36, no. 5, pp. 2360 – 8, 2008.

[83] Y. Miyake and H. Usui, "New electromagnetic particle simulation code for the analysis of spacecraft-plasma interactions," *Phys. Plasmas*, vol. 16, no. 6, p. 062904 (11 pp.), 2009.

[84] S. Markidis, G. Lapenta, and Rizwan-uddin, "Multi-scale simulations of plasma with ipic3d," *Math. Comput. Simul.*, vol. 80, no. 7, pp. 1509 – 19, 2009.

[85] R. Ergun, D. Malaspina, S. Bale, J. McFadden, D. Larson, F. Mozer, N. Meyer-Vernet, M. Maksimovic, P. Kellogg, and J. Wygant, "Spacecraft charging and ion wake formation in the near-sun environment," *Phys. Plasmas*, vol. 17, no. 7, p. 072903 (9 pp.), 2010.

[86] K. M. Frederick-Frost and K. Lynch, "Low energy stable plasma calibration facility," *Rev. Sci. Instrum.*, vol. 78, no. 7, p. 075113 (9 pp.), 2007.

[87] L. Gayetsky and K. Lynch, "Note: Flowing ion population from a resonance cavity source," *Rev. Sci. Instrum.*, vol. 82, no. 4, p. 046112 (3 pp.), 2011.